

AD-A061 596

NATIONAL OCEANIC AND ATMOSPHERIC ADMINISTRATION BOUL--ETC F/G 4/2
MEASUREMENTS SHOWING THE FEASIBILITY FOR RADAR DETECTION OF HAZ--ETC(U)
FEB 78 R B CHADWICK, K P MORAN, G E MORRISON Y77-847

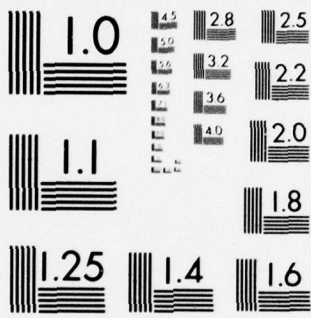
UNCLASSIFIED

AFOL-TR-78-0160

NL

| OF |
AD
A061596





MICROCOPY RESOLUTION TEST CHART
NATIONAL BUREAU OF STANDARDS-1963-A

DDC FILE COPY

AD A061596

LEVEL II

12

18

AFGL TR-78-0160

19

MEASUREMENTS SHOWING THE FEASIBILITY FOR
RADAR DETECTION OF HAZARDOUS WIND SHEAR
AT AIRPORTS

10

R. B. Chadwick,
K. P. Moran,
G. E. Morrison
W. C. Campbell

National Oceanic and Atmospheric Administration (NOAA)
Meteorological Radar Program Area
Wave Propagation Laboratory
Boulder, CO 80302

9

Final Report.
1 Nov 1976 - 28 Feb 1978

11

28 Feb 78

12

89 P.

Approved for public release distribution unlimited.

15

Y77-847

This research was supported by the Air Force In-House
Laboratory Independent Research Fund

16

1LIR

17

76

AIR FORCE GEOPHYSICS LABORATORY
AIR FORCE SYSTEMS COMMAND
UNITED STATES AIR FORCE
HANS COM AFB, MASSACHUSETTS 01731

DDC
RECEIVED
NOV 28 1978
D

406 292

20

059

mt

Qualified requestors may obtain additional copies from the Defense Documentation Center. All others should apply to the National Technical Information Service.

Unclassified

SECURITY CLASSIFICATION OF THIS PAGE (When Data Entered)

REPORT DOCUMENTATION PAGE		READ INSTRUCTIONS BEFORE COMPLETING FORM
1. REPORT NUMBER AFGL-TR-78-0160	2. GOVT ACCESSION NO.	3. RECIPIENT'S CATALOG NUMBER
4. TITLE (and Subtitle) MEASUREMENTS SHOWING THE FEASIBILITY FOR RADAR DETECTION OF HAZARDOUS WIND SHEAR AT AIRPORTS		5. TYPE OF REPORT & PERIOD COVERED Final Report 1 Nov 1976 - 28 Feb 1978
		6. PERFORMING ORG. REPORT NUMBER
7. AUTHOR(s) R.B. Chadwick G.E. Morrison K.P. Moran W.C. Campbell		8. CONTRACT OR GRANT NUMBER(s) Y77-847
9. PERFORMING ORGANIZATION NAME AND ADDRESS NOAA/ERL/Wave Propagation Laboratory Boulder, CO 80302		10. PROGRAM ELEMENT, PROJECT, TASK AREA & WORK UNIT NUMBERS 61101F ILIR7GAA
11. CONTROLLING OFFICE NAME AND ADDRESS Air Force Geophysics Laboratory (LYW) Hanscom AFB, Massachusetts 01731 Monitor/Ralph Donaldson/LYW		12. REPORT DATE 21 June 1978
		13. NUMBER OF PAGES 92
14. MONITORING AGENCY NAME & ADDRESS (if different from Controlling Office)		15. SECURITY CLASS. (of this report) Unclassified
		15a. DECLASSIFICATION/DOWNGRADING SCHEDULE
16. DISTRIBUTION STATEMENT (of this Report) Approved for public release; distribution unlimited.		
17. DISTRIBUTION STATEMENT (of the abstract entered in Block 20, if different from Report)		
18. SUPPLEMENTARY NOTES This research was supported by the Air Force In-House Laboratory Independent Research Fund		
19. KEY WORDS (Continue on reverse side if necessary and identify by block number) Wind Shear C _n ² Measurements Clear Air Radar FM-CW Doppler Radar		
20. ABSTRACT (Continue on reverse side if necessary and identify by block number) Measurements of the strength of clear-air backscattered power for a 10 cm radar were made over a 12 month period in Colorado. The main conclusion is that radar offers a viable option for warning of hazardous low-level wind shear at airports. There were 161 days of operation and diurnal and seasonal trends of the return are identified. It is shown that the back- scattered power can be considered as a single parameter log-normal random variable. The problems encountered in low elevation angle operation are discussed and one solution, a clutter suppression system is presented.		

DD FORM 1 JAN 73 1473

EDITION OF 1 NOV 65 IS OBSOLETE

Unclassified

SECURITY CLASSIFICATION OF THIS PAGE (When Data Entered)

LEVEL II

12

CONTENTS

	Page
1. Introduction	1
2. Radar calibration and calculations	2
2.1 Electronic calibration	3
2.2 Antenna calibration	4
2.3 C_n^2 calculations	6
3. C_n^2 measurements	9
3.1 Mode of operation	9
3.2 Time ordered histograms	10
3.3 Combined histograms	17
3.4 Combined hour-of-the-day histograms	27
3.5 Probability law for C_n^2	29
3.6 Comparison with in-situ measurements	32
4. Operation at low elevation angles	33
4.1 Plan shear indicator (PSI) display	34
4.2 Ground clutter suppressors	38
4.3 Sweep frequency stabilizer	41
5. Other activities	44
5.1 Radio acoustic sounding system (RASS)	45
5.2 Wake vortex detection	46
5.3 Radar operation over phone lines	47
6. Conclusions	47
7. References	49

ACCESSION BY	
DTIC	Write Section <input checked="" type="checkbox"/>
DDC	DDC Section <input type="checkbox"/>
CLASSIFIED	<input type="checkbox"/>
JUSTIFICATION	
BY	
DISTRIBUTION/AVAILABILITY CODES	
COL	AVAIL. and/or SPECIAL
A	

DDC
RECEIVED
NOV 28 1978
RECEIVED

RECEIVED PAGE NOT FILMED
BLACK

CONTENTS (continued)

	Page
8. Appendices	
A. A Simplified Explanation for Processing of FM-CW Doppler Radar Signals from Distributed Targets	A1
B. Required Frequency Stability to Suppress Ground Clutter. .	B1
C. Comparison of Clutter Power for a Pulse Radar and a CW Radar	C1
D. Histograms of C_n^2	D1

MEASUREMENTS SHOWING THE FEASIBILITY FOR RADAR DETECTION
OF HAZARDOUS WIND SHEAR AT AIRPORTS

R. B. Chadwick, K. P. Moran,
G. E. Morrison, and W. C. Campbell
NOAA/ERL/Wave Propagation Laboratory
Boulder, Colorado 80302

1. Introduction

The most hazardous aspects of aviation are the landing and take-off when both airspeed and altitude are necessarily small. At these times aircraft are the most vulnerable to small scale meteorological phenomena. In recent years, the hazards of low level wind shear have become apparent and some crashes that previously would have been attributed to "pilot error," are now recognized as due to wind shear. How many crashes are wind shear related is not known. However, Fujita and Caracena (1977) analyzed three commercial airline crashes that occurred in 1975 and 1976 and determined that they were due to wind shear.

There are several remote sensing techniques that could be used to measure wind shear at an airport. Which one is "best" depends on the requirements for an operational wind shear detection system. These requirements depend in turn on the structure of the meteorological phenomenon that causes the hazardous wind shear. Fujita and Caracena (1977) found the hazardous wind shear was caused by an intense, localized downdraft, which they term a "downburst." They found that the hazardous area may be only a few km across and can move horizontally very fast. On the basis of this, a reasonable requirement for a wind shear detection system is that it be capable of measuring shear in the air volume in which the aircraft will be vulnerable to wind shear. This capability would require measurement along the glide path from the mid-point of the runway to a range where the aircraft would have sufficient altitude to recover from a "downburst." From the data on actual crashes and near

crashes given by Fujita and Caracena (1977), a range of 10,000 feet would be required. An adequate safety margin might increase this to 15,000 ft or about 5 km.

One remote sensor that has potential for meeting these requirements is the FM-CW Doppler radar. (An explanation of the principle behind this type of radar is given in Appendix A.) The Wave Propagation Laboratory FM-CW radar is contained on two trailers which can be relocated in one day. The system uses two 8-foot antennas which can be scanned in a hemisphere. The wavelength is 10 cm and the transmitted power is 200 W. When hydrometeors are present, they act as tracers of the wind; however, the radar has sufficient sensitivity to detect backscatter from the refractive-index fluctuations in the clear air. These turbulence-induced fluctuations then act as tracers of the wind. Since attenuation is small at these frequencies, the system has all-weather capability.

This report describes an experiment designed to test the feasibility of using an FM-CW Doppler radar to detect hazardous wind shear. The main output of the experiment is the collection of strength-of-return data as a function of time of day and month, and these data are presented in such a way as to be applicable for any electromagnetic backscatter radar. An explanation of how the radar was calibrated to obtain these data is given in Section 2. The strength-of-return data are presented in histogram form in Section 3 and Appendix D. A second goal of the experiment was to attempt radar operation at low elevation angles and this is discussed in Section 4. The results of three other related activities are discussed in Section 5 and conclusions are presented in Section 6.

2. Radar Calibration and Calculations

It is generally not necessary to calibrate an FM-CW Doppler radar to make velocity or wind shear measurements. However calibration is required to make the strength-of-return measurements reported here. For a dual antenna radar, two types of calibration are required. First, the electronic portion of the radar must be calibrated so that the area

under a Doppler spectrum can be related to the received power associated with that spectrum. Second, since the effective antenna pattern is actually the overlap between the transmitting and receiving antennas, this overlap must be quantified. The next two sections discuss these calibrations and the last section discusses how the calibrated return power is related to C_n^2 , the atmospheric parameter of interest in clear air wind measurement.

2.1 Electronic Calibration

The basic idea in calibration of the electronic portion of our radar is to inject a known test signal into the receiver. Then the proportionality constant between received power and radar output can be determined. Two different configurations were used to obtain the test signal. The first was to take the test signal from the output of the high power transmitter and return it to the receiver trailer by coaxial cable. The major difficulty with this arrangement was that the attenuation of this coaxial cable changed with temperature. The temperature changes were caused mainly by the sun heating the cable. To avoid this problem we took the test signal from inside the trailer so that any coaxial cable was not in the sun. This necessitated using a power monitor to measure and record the transmitted power. A block diagram of the calibration arrangement we used most of the time is shown in Fig. 2.1.

The calibration procedure (which was performed usually once per day) is to turn off the TWT, connect the test signal, and then record one record out of the signal processor. Then the test signal is disconnected and a second record is recorded to give a noise baseline with no input. One record is then subtracted from the other and the difference (in the 10 μ s range cell) is the spectrum of the test signal. Since the strength of the test signal is known (from the power meter reading) and the area under the test signal spectrum is known, the proportionality constant relating spectral area to received power can be found.

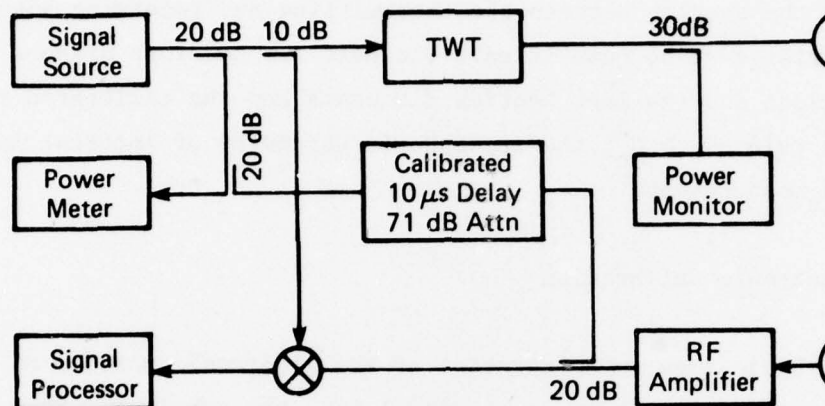


Figure 2.1. FM-CW radar calibration subsystem.

The only difficulty with this approach is that the RF low noise amplifier is not in the calibration loop. Gain changes in this amplifier were kept to a minimum by a constant temperature heater. The gain was checked periodically to monitor any long term changes. The main calibration error is probably due to unknown gain changes in this RF amplifier and we believe that the unknown changes are 2 dB.

2.2 Antenna Calibration

Since the FM-CW radar uses separate antennas for transmitting and receiving, an unconventional calibration and measurement procedure must be used. First, we measured antenna patterns using conventional antenna range techniques. The patterns for the two antennas were very nearly identical and one of the measured patterns is shown in Fig. 2.2. Then we used an analytical argument to show how this single pattern is changed into an effective antenna pattern that is a function of range as well as angle.

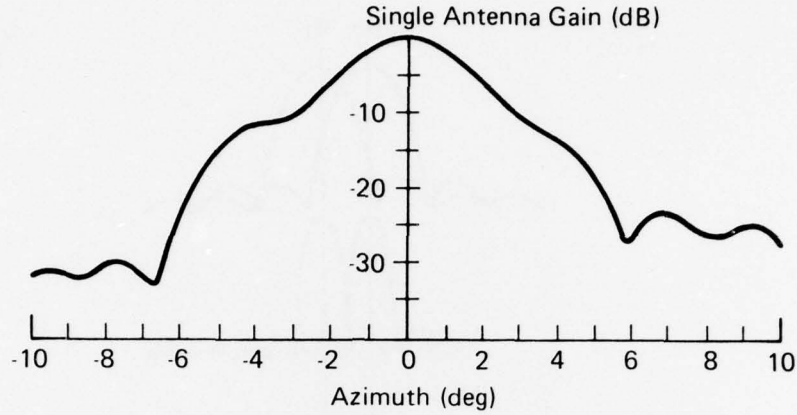


Figure 2.2. Antenna pattern for receiving antenna.

The antennas beams point in parallel directions, so there is only a small overlap at close ranges and complete overlap at long ranges. This overlap is characterized by multiplying one antenna pattern by the other and integrating the result. Assume the two antennas are separated by a distance D and are pointed in parallel directions as shown in Fig. 2.3. Define $F(R)$, the overlap at range R , as the integral of the product of the two antenna patterns. Using small-angle approximations in Fig. 2.3, we see that

$$F(R) = \frac{C}{R} \int_{-\infty}^{\infty} G_1\left(\frac{W + \frac{D}{2}}{R}\right) G_2\left(\frac{W - \frac{D}{2}}{R}\right) dW$$

where the term outside the integral is necessary to insure the boundary conditions of the overlap. We require that $F(R \rightarrow 0) = 0$ and $F(R \rightarrow \infty) = 1$. Evaluating the constant and changing the variable of integration we obtain

$$F(R) = \frac{\int G_1\left(\theta + \frac{D}{2R}\right) G_2\left(\theta - \frac{D}{2R}\right) d\theta}{\int G_1(\theta) G_2(\theta) d\theta} .$$

But this is just the normalized cross-correlation function between the two antenna patterns, and in our case, since the two antenna patterns are

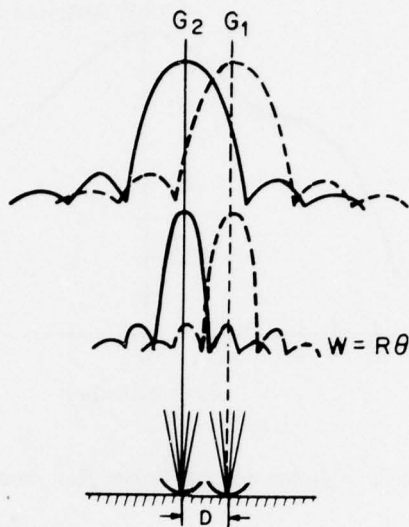


Figure 2.3. Beam overlap for two antennas.

equal, this becomes the autocorrelation function, $R_G(\cdot)$. So, the overlap is given by

$$F(R) = R_G\left(\frac{D}{R}\right).$$

The overlap can be calculated with lagged products and is shown in Fig. 2.4.

In any return strength of signal calculation, the effects of the antenna overlap can be taken into account by simply multiplying either the antenna pattern or the effective area by $F(R)$. This was done in all of our calculations.

2.3 C_n^2 Calculations

Once the radar is calibrated, the return power for each range cell can be determined, but these results would apply only to our radar. A better approach is to calculate a pertinent atmospheric parameter that would be applicable to other radars as well. For clear air radar scattering

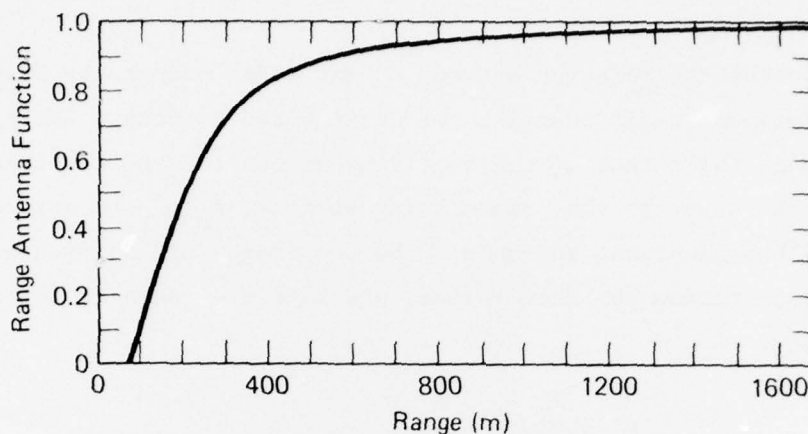


Figure 2.4. Range antenna function.

the best atmospheric parameter is the structure constant of radio refractive-index, which is generally denoted as C_n^2 and has units of $m^{-2/3}$. If the atmospheric turbulence is homogeneous and isotropic and $n(r_0)$ is the refractive-index at position r_0 , then C_n^2 is defined by

$$\overline{[n(r_0) - n(r_0 + r)]^2} = C_n^2 r^{2/3},$$

where r is the separation distance between two points. Whenever the scale size of interest, $\lambda/2$, lies within the inertial subrange of turbulence, the radar cross-section per unit volume, η , is given by, (Ottersten, 1969)

$$\eta = 0.38 C_n^2 \lambda^{-1/3}.$$

The inertial subrange lies between the inner and outer scale of turbulence, and in the boundary layer the inner scale is on the order of a mm. The outer scale is determined by atmospheric stability; for high stability this outer scale is about 5 m and under convective conditions, it increases to perhaps 2 km. So the C_n^2 values given here should be useful for any conceivable radar application in the boundary layer.

To derive the relation between C_n^2 and radar output, we start with the conventional radar equation for distributed targets. Let P_r be the power at the output of the receiving antenna; P_T be the transmitted power at the input to the transmitting antenna; A_e be the effective area of one of the identical antennas; Δ be the range cell size; η be the radar cross section per unit volume; and R be the range of interest. Then we have

$$P_r = \frac{P_T A_e \Delta \eta}{4\pi R^2} .$$

However, the overlap of the antenna beams discussed in the previous section must be included to adjust for lack of intersection at lower ranges. This gives

$$P_r = \frac{P_T R_G \left(\frac{D}{R}\right) A_e \Delta \eta}{4\pi R^2} .$$

Solving for C_n^2 after substituting for η we obtain

$$C_n^2 = \frac{P_r}{P_T} \frac{33}{R_G \left(\frac{D}{R}\right)} \frac{R^2}{\Delta} \frac{\lambda^{1/3}}{A_e} .$$

Now, since the target fills the beam, we must make a correction since the antenna gain at the edges of the beam is different than that at the center (Probert-Jones, 1962). Also we use $\lambda = .1$ m and $A_e = 2.52$ m to obtain

$$C_n^2 = \frac{8.43}{R_G \left(\frac{D}{R}\right)} \frac{P_r}{P_T} \frac{R^2}{\Delta} .$$

The only thing left is to insert the calibration of the radar receiver and signal processor so that P_r can be replaced by a quantity from the output of the radar. Let A_r be that quantity which is equal to the area under the velocity spectrum for the range of interest. Also let A_s be

the area under the velocity spectrum of the test signal which has power P_s . It is then clear that

$$\frac{P_r}{A_r} = \frac{P_s}{A_s}$$

and the equation for C_n^2 becomes

$$C_n^2 = \frac{8.43}{R_G \left(\frac{D}{R}\right)} \frac{A_r}{A_s} \frac{P_s}{P_T} \frac{R^2}{\Delta} \text{ (meters)}^{-2/3}.$$

Note that the units on A_r and A_s are unimportant since they cancel. This is the equation that was used to calculate the measured C_n^2 values given in the next section.

3. C_n^2 Measurements

The radar made C_n^2 measurements from March, 1977 through February 1978. During the spring and summer, we attempted to take data continuously, and we failed only during periods of transporting the radar or during periods of equipment failure. During the late fall and winter, we took data on an intermittent basis because the radar computer was being used for processing data.

3.1 Mode of Operation

During the entire experiment, we deviated only slightly from a fairly standard mode of operation. The radar antennas were pointed at an elevation angle of 60° - 75° and the azimuth was any convenient value, since the height and height resolution is unaffected by the azimuth angle. The frequency was generally just a few MHz below 3 GHz, and the transmitted power was approximately 200 W. The sweep length was generally 3 ms, and 50 sweeps were coherently processed. From Appendix A we see that this means the output has a 50 point velocity spectrum for each of 10 range cells.

Because of power line harmonics, we did not attempt to process the data in the lowest range bin and this left 9 range cells of length 161 m each. The spectra were recorded on magnetic tape, and the calculations to extract C_n^2 values were performed off-line.

A record of data consists of 500 data points (ten 50-point velocity spectra) and one record was recorded every 60 seconds. Each record was a running average of the radar output over approximately 60 seconds. In the off-line processing programs the C_n^2 value for each range cell was calculated for each of the 1-minute records as described in the previous section. This resulted in 60 C_n^2 measurements at that range for each hour of operation, and these 60 measurements were used to form a histogram of C_n^2 values. The histograms were written onto a compressed data tape which was used to study histograms as functions of height or time or hour of the day.

3.2 Time Ordered Histograms

In the Boulder, Colorado, area over the past two years we have observed that C_n^2 in the boundary layer can vary over a 63 dB range. Because of this large range, the histogram variable is $-\log_{10} C_n^2$ rather than C_n^2 . For each decade of C_n^2 values, three histogram bins were formed. For example, a C_n^2 bin extends from 1×10^{-15} to $2.15 \times 10^{-15} m^{-2/3}$. The next higher bin extends from 2.15×10^{-15} to $4.64 \times 10^{-15} m^{-2/3}$ and the next higher from 4.64×10^{-15} to $10 \times 10^{-15} m^{-2/3}$. This results in three equal sized bins on a logarithmic scale and is repeated for each decade of C_n^2 values.

Figure 3.1 is a sequence of hourly histograms that extend over a two-week period. The five columns of numbers on the left are month, day, year, hour, and minute. The row of numbers extending from 11 to 19 are $-\log_{10} C_n^2$ where each decade has been broken into three bins as described above. The 1-hour histograms are shown as rows across the page where each number represents how many 1-minute measurements of C_n^2 fell into that bin of values during the hour. This figure shows the hour-to-hour and day-to-day variation of a typical set of C_n^2 data.

```

***** RANGE FOR THIS CELL IS = 805 METERS *****
DATE: MONTH/DAY/YEAR 5/14/77
TIME: HOURS:MINUTES:SECONDS 11:41:55
10.0 2.15 FILE 9 REC 38
11 11 11 12 12 12 13 13 13 14 14 15 15 15 16 16 16 17 17 17
5 14 77 11 41 7 19 15 16 3
5 14 77 12 42 10 13 23 12 1 1
5 14 77 13 42 44 16
5 14 77 14 43 2 11 8 6 30 3
5 14 77 15 43 10 13 37
5 14 77 16 43 15 9 22 14
5 14 77 17 44 1 9 7 8 20 11 4
5 14 77 18 44 2 37 21
5 14 77 19 45 40 19 1
5 14 77 20 47 19 29 9 3
5 14 77 21 49 1 5 7 23 20 3 1
5 14 77 22 51 4 26 14 13 2 1
5 14 77 23 53 7 9 18 8 12 6
5 15 77 0 54 12 37 10 1
5 15 77 1 55 20 37 3
5 15 77 2 57 3 15 6 16 9 6 4
5 15 77 4 0 19 17 5 4 6 6 2 1
5 15 77 5 2 5 41 10 3 1
5 15 77 6 4 1 33 20 6
5 15 77 7 6 16 34 9 1
5 15 77 8 9 11 45 4
5 15 77 9 10 23 26 2 5 4
5 15 77 10 10 4 37 7 4 2 2 1 1 1
5 15 77 11 10 3 38 7 2 7 2 1
5 15 77 12 10 41 15 1 1 2
5 15 77 13 11 1 50 9
5 15 77 14 11 14 35 10 1
5 15 77 15 11 13 31 15 1
5 15 77 16 12 17 23 17 3
5 15 77 17 12 4 15 40 1
5 15 77 18 12 11 46 3
5 15 77 19 13 3 47 10
5 15 77 20 13 1 10 4 5 33 7
5 15 77 21 13 23 12 24 1
5 15 77 22 14 4 48 8
5 15 77 23 14 8 39 13
5 16 77 0 14 1 19 29 11
5 16 77 1 15 28 32
5 16 77 2 15 6 40 12 1
5 16 77 3 15 58 2
5 16 77 4 16 24 34 1 1
5 16 77 5 16 1 26 21 9 3
5 16 77 6 18 3 28 27 2
5 16 77 7 19 3 57
5 16 77 8 20 35 25
5 16 77 9 20 2 51 6 1
5 16 77 10 20 1 43 16
5 16 77 11 21 23 36 1
5 16 77 12 21 19 38 2 1
5 16 77 13 21 36 20 3
5 16 77 14 22 32 28
5 16 77 15 22 34 24 2
5 16 77 16 22 4 29 27
5 16 77 17 23 27 33
5 16 77 18 23 1 48 11

```

Figure 3.1(a). Hourly histograms of C_n^2 at 805 m.

```

***** RANGE FOR THIS CELL IS = 805 METERS *****
DATE: MONTH/DAY/YEAR 5/16/77
TIME: HOURS:MINUTES:SECONDS 19:23:53
10 0 4.64 2.15 FILE 9 REC 94
11 11 11 12 12 12 13 13 13 14 14 14 15 15 15 16 16 16 17 17 17
5 16 77 19 23 5 53 2
5 16 77 20 24 11 42 7
5 16 77 21 24 5 35 17 3
5 16 77 22 24 3 7 42 6 1 1
5 16 77 23 25 15 40 5
5 17 77 0 25 3 29 27 1
5 17 77 1 26 4 22 28 2 2 2
5 17 77 2 26 23 34 2 1
5 17 77 3 27 20 36 4
5 17 77 4 29 11 32 15 2
5 17 77 5 31 3 9 29 18 1
5 17 77 6 33 2 58
5 17 77 7 34 30 30
5 17 77 8 35 1 9 46 4
5 17 77 9 35 14 45 1
5 17 77 10 35 2 56 2
5 17 77 11 36 4 56
5 17 77 12 36 25 34 1
5 17 77 13 36 32 28
5 17 77 14 37 1 54 5
5 17 77 15 37 24 34 2
5 17 77 16 37 7 52 1
5 17 77 17 38 4 47 9
5 17 77 18 38 15 11 29 5
5 17 77 19 38 34 26
5 17 77 20 39 43 17
5 17 77 21 39 2 12 37 6 2 1
5 17 77 22 39 1 4 14 24 12 2 2 1
5 17 77 23 40 4 14 33 7 1 1
5 18 77 0 40 1 11 26 9 8 5
5 18 77 1 40 17 34 7 1 1
5 18 77 2 41 18 25 4 6 3 1 1
5 18 77 3 41 36 21 2 1
5 18 77 4 41 15 42 3
5 18 77 5 43 5 30 24 1
5 18 77 6 45 17 22 21
5 18 77 7 46 11 29 5 15
5 18 77 8 46 5 39 16
5 18 77 9 46 2 26 24 8
5 18 77 10 49 6 21 3 24 3
5 18 77 11 49 19 36 5
5 18 77 12 49 7 27 26
5 18 77 13 50 9 29 18 4
5 18 77 14 50 15 34 10 1
5 18 77 15 50 6 15 31 6 2
5 18 77 16 50 4 31 21 4
5 18 77 17 51 2 22 25 10 1
5 18 77 18 51 3 12 39 6
5 18 77 19 51 6 10 18 15 8 1 1
5 18 77 20 52 3 21 35 1
5 18 77 21 52 5 37 11 4 2 1
5 18 77 22 52 14 41 4 1
5 18 77 23 53 2 30 26 2
5 19 77 0 53 1 9 39 9 1 1
5 19 77 1 53 3 16 24 15 2

```

Figure 3.1(b). Hourly histograms of C_n^2 at 805 m.

```

***** RANGE FOR THIS CELL IS = 805 METERS *****
DATE: MONTH/DAY/YEAR 5/19/77
TIME: HOURS:MINUTES SECONDS 2:54:17
      10 0      4.64      2.15  FILE 9  REC 149
      11 11 11 12 12 12 13 13 13 14 14 14 15 15 15 16 16 16 17 17 17
5 19 77 2 54
5 19 77 3 54
5 19 77 4 54
5 19 77 5 55
5 19 77 6 55
5 19 77 7 55
5 19 77 8 56
5 19 77 9 56
5 19 77 10 27
5 19 77 11 27
5 19 77 12 27
5 19 77 13 28
5 19 77 14 28
5 19 77 15 28
5 19 77 16 29
5 19 77 17 29
5 19 77 18 29
5 19 77 19 30
5 19 77 20 30
5 19 77 21 30
5 19 77 22 31
5 19 77 23 31
5 20 77 0 31
5 20 77 1 32
5 20 77 2 32
5 20 77 3 32
5 20 77 4 33
5 20 77 5 33
5 20 77 6 33
5 20 77 7 33
5 20 77 8 34
5 20 77 9 34
5 20 77 10 35
5 20 77 11 35
5 20 77 12 35
5 20 77 13 36
5 20 77 14 36
5 20 77 15 36
5 20 77 16 37
5 20 77 17 37
5 20 77 18 37
5 20 77 19 38
5 20 77 20 38
5 20 77 21 38
5 20 77 22 39
5 20 77 23 39
5 21 77 0 39
5 21 77 1 40
5 21 77 2 40
5 21 77 3 40
5 21 77 4 41
5 21 77 5 41
5 21 77 6 41
5 21 77 7 42
5 21 77 8 42
      7 7 20 24 2
      5 30 22 3
      7 30 23
      4 24 30 2
      2 8 29 19 2
      3 42 14 1
      19 27 14
      18 39 3
      14 26 11 6
      8 21 29 2
      2 34 24
      3 24 26 7
      1 19 40
      21 33 6
      2 7 34 15 1 1
      1 1 5 46 7
      2 3 1 2 15 36 1
      2 35 15 8
      2 10 21 21 6
      29 19 6 6
      5 17 21 13 3 1
      2 35 19 4
      3 24 26 4 1 2
      2 11 8 23 12 2 2
      8 28 20 3 1
      1 2 24 29 4
      4 17 32 7
      3 11 28 17 1
      9 8 1 1 5 12 18 4 1 1
      1 7 23 4 10 15
      8 21 1 6 15 9
      19 26 9 5 1
      14 35 8 3
      13 39 8
      11 39 10
      4 15 7 2 24 7 1
      6 15 11 20 8
      5 18 13 12 8 3 1
      4 5 49 2
      7 14 30 9
      9 3 5 14 12 13 4
      1 11 31 15 2
      13 7 31 9
      1 12 20 17 10
      6 12 22 16 2 2
      10 26 23 1
      10 40 10
      1 8 36 13 2
      10 29 13 8
      4 53 3
      26 27 7
      5 18 28 9
      8 27 18 7
      2 1 44 13
      12 48

```

Figure 3.1(c). Hourly histograms of C_n^2 at 805 m.


```

***** RANGE FOR THIS CELL IS = 805 METERS *****
DATE: MONTH/DAY/YEAR 5/21/77
TIME: HOURS:MINUTES:SECONDS 9:42:45
      10.0      4.64      2.15  FILE 9  REC 205
      11 11 11 12 12 12 13 13 13 14 14 14 15 15 15 16 16 16 17 17 17
5 21 77 9 42      4 44 12
5 21 77 10 43      1 31 27 1
5 21 77 11 43      1 35 24
5 21 77 12 43      6 28 15 11
5 21 77 13 44      1 1 4 6 26 19 3
5 21 77 14 44      36 23 1
5 21 77 15 44      2 51 7
5 21 77 16 45      3 10 13 25 7 2
5 21 77 17 45      3 22 27 8
5 21 77 18 45      2 5 7 4 13 21 6 2
5 21 77 19 45      11 40 9
5 21 77 20 46      1 3 8 10 20 16 2
5 21 77 21 46      14 21 16 9
5 21 77 22 46      2 29 25 4
5 21 77 23 47      14 30 14 2
5 22 77 0 47      5 33 21 1
5 22 77 1 47      1 27 29 3
5 22 77 2 48      2 36 22
5 22 77 2 48      2 36 22
5 22 77 10 19      3 18 37 1
5 22 77 11 19      60
5 22 77 12 20      4 53 3
5 22 77 13 20      22 25 12 1
5 22 77 14 20      7 34 19
5 22 77 15 21      24 35 1
5 22 77 16 21      12 48
5 22 77 17 22      7 42 11
5 22 77 18 22      12 25 23
5 22 77 19 22      2 39 19
5 22 77 20 23      1 57 2
5 22 77 21 23      11 17 31 1
5 22 77 22 23      2 57 1
5 22 77 23 24      52 2 1 1 1 1 1
5 23 77 0 24      18 41 1
5 23 77 1 25      37 23
5 23 77 2 25      12 47 1
5 23 77 3 25      9 45 6
5 23 77 4 26      17 18 9 15 1
5 23 77 5 26      1 1 3 16 37 2
5 23 77 6 26      25 15 17 3
5 23 77 7 27      3 45 12
5 23 77 8 27      1 20 34 5
5 23 77 9 27      2 55 3
5 23 77 10 28      19 41
5 23 77 11 28      2 56 2
5 23 77 12 28      1 25 30 3 1
5 23 77 13 29      56 1 1 1 1
5 23 77 14 29      30 30
5 23 77 15 30      52 8
5 23 77 16 30      55 5
5 23 77 17 30      14 42 4
5 23 77 18 31      49 11
5 23 77 19 31      40 20
5 23 77 20 32      21 38 1
5 23 77 21 32      15 45

```

Figure 3.1(d). Hourly histograms of C_n^2 at 805 m.

```

***** RANGE FOR THIS CELL IS = 805 METERS *****
DATE: MONTH/DAY/YEAR 5/23/77
TIME: HOURS: MINUTES: SECONDS 22:32:48
10.0 4.64 2.15 FILE 10 REC 38
11 11 11 12 12 12 13 13 13 14 14 14 15 15 15 16 16 16 17 17 17
5 23 77 22 32 9 43 8
5 23 77 23 33 44 16
5 24 77 0 33 1 24 35
5 24 77 1 33 8 52
5 24 77 2 34 43 17
5 24 77 3 34 3 42 15
5 24 77 4 35 1 19 23 16 1
5 24 77 5 35 3 40 14 3
5 24 77 6 35 3 50 6 1
5 24 77 7 36 9 50 1
5 24 77 8 36 53 7
5 24 77 9 36 26 34
5 24 77 10 36 13 45 2
5 24 77 11 37 42 18
5 24 77 12 37 49 11
5 24 77 13 38 5 28 25 2
5 24 77 14 38 8 33 18 1
5 24 77 15 38 3 14 32 11
5 24 77 16 38 1 47 12
5 24 77 17 39 10 34 16
5 24 77 18 39 5 35 20
5 24 77 19 39 16 36 7 1
5 24 77 20 40 1 59
5 24 77 21 40 4 25 27 4
5 24 77 22 41 4 15 32 9
5 24 77 23 41 42 10 6 1 1
5 25 77 0 41 31 29
5 25 77 1 42 20 39 1
5 25 77 2 42 2 55 3
5 25 77 3 42 8 46 6
5 25 77 4 43 4 26 22 8
5 25 77 5 43 6 50 4
5 25 77 6 43 2 45 13
5 25 77 7 44 10 33 16 1
5 25 77 8 44 22 29 7 2
5 25 77 9 44 29 31
5 25 77 10 45 2 15 25 18
5 25 77 11 45 28 32
5 25 77 12 45 1 32 27
5 25 77 13 46 28 32
5 25 77 14 11 2 32 21 2 2 1
5 25 77 15 11 5 49 6
5 25 77 16 11 12 42 6
5 25 77 17 12 6 27 22 3 1 1
5 25 77 18 12 5 19 14 9 4 7
5 25 77 19 12 6 3 1 1 6 12 10 11 6 3
5 25 77 20 13 3 12 8 6 5 9 6 9 1 1
5 25 77 21 13 2 8 17 14 2 6 3 6 2
5 25 77 22 13 1 16 34 7 1
5 25 77 23 14 6 36 18
5 26 77 0 14 7 17 21 13 2
5 26 77 1 14 17 38 5
5 26 77 2 15 18 37 5
5 26 77 3 15 6 46 8
5 26 77 4 15 5 14 22 9 1 5 4

```

Figure 3.1(e). Hourly histograms of C_n^2 at 805 m.

```

***** RANGE FOR THIS CELL IS = 805 METERS *****
DATE: MONTH/DAY/YEAR 5/26/77
TIME: HOURS:MINUTES:SECONDS 5:15:58
10.0 4.64 2.15 FILE 10 REC 93
11 11 11 12 12 12 13 13 13 14 14 14 15 15 15 16 16 16 17 17 17
5 26 77 5 15 1 1 1 8 19 12 10 7
5 26 77 6 16 2 4 19 31 4
5 26 77 7 16 2 26 31 1
5 26 77 8 16 12 46 2
5 26 77 9 16 1 12 14 21 10 2
5 26 77 10 17 4 20 21 13 2
5 26 77 11 17 1 45 14
5 26 77 12 17 1 8 34 13 2 1 1
5 26 77 13 17 5 29 21 4 1
5 26 77 14 18 2 29 28 1
5 26 77 15 18 3 47 10
5 26 77 16 18 2 2 2 28 15 5 2 1 1 1 1
5 26 77 17 19 9 11 8 3 3 6 9 9 2
5 26 77 18 19 24 27 7 2
5 26 77 19 19 6 11 5 13 6 8 8 3
5 26 77 20 20 1 5 27 25 2
5 26 77 21 20 1 6 20 9 7 16 1
5 26 77 22 20 1 32 21 4 2
5 26 77 23 21 8 32 19 1
5 27 77 0 21 1 1 30 23 5
5 27 77 1 21 37 20 3
5 27 77 2 22 18 42
5 27 77 3 22 1 43 15 1
5 27 77 4 23 3 37 15 5
5 27 77 5 23 20 37 3
5 27 77 6 23 13 36 11
5 27 77 7 23 18 38 4
5 27 77 8 23 8 40 12
5 27 77 9 24 14 38 8
5 27 77 10 24 18 26 16
5 27 77 11 24 3 15 34 3 2 1 1
5 27 77 12 24 9 20 21 7 3
5 27 77 13 25 7 18 24 7 4
5 27 77 14 39 3 5 21 18 9 3 1
5 27 77 15 40 2 11 17 15 10 5
5 27 77 16 40 3 8 1 6 17 23 1 1
5 27 77 17 40 48 12
5 27 77 18 40 4 12 28 16
5 27 77 19 41 24 36
5 27 77 20 41 21 39
5 27 77 21 41 1 3 35 3 10 8
5 27 77 22 42 1 27 11 18 3
5 27 77 23 42 5 21 29 5
5 28 77 0 42 10 23 25 2
5 28 77 1 43 16 43 1
5 28 77 2 43 7 42 9 1 1
5 28 77 3 44 8 12 18 14 8
5 28 77 4 44 1 4 14 36 5
5 28 77 5 44 1 2 8 9 8 16 16
5 28 77 6 45 4 3 8 4 9 16 6 7 3
5 28 77 7 45 1 1 1 16 30 11
5 28 77 8 45 3 16 16 16 9
5 28 77 9 46 2 1 5 9 28 9 4 1 1
5 28 77 10 46 1 4 19 30 6
5 28 77 11 46 3 36 19 1 1

```

Figure 3.1(f). Hourly histograms of C_n^2 at 805 m.

3.3 Combined Monthly Histograms

The monthly variation of C_n^2 can be found by combining hourly histograms for each month and these are shown in Appendix D. These histograms contain the effects of birds, insects, airplanes, rain, and snow storms, etc. Thus, the upper (leftmost) part of the histogram can not be attributed completely to clear air return. However, it is likely that the lower part of the histogram is relatively free of these other targets. Figure 3.2 shows C_n^2 data obtained by integrating the lower part of the histograms to obtain three values, one that will be greater than C_n^2 5% of the time, a second that will be greater than C_n^2 30% of the time, and a third that will be greater than C_n^2 50% of the time. In Figure 3.2 these levels are plotted, for each of the nine range cells, as a function of month.

One surprising feature of Figure 3.2 is the drop from June to July, since one would expect similar returns in June and July. One possible explanation for this drop is that the radar was moved to a different location. The March to June data were taken near Boulder, Colorado, near large areas of irrigated farmland. The July to October data were taken at Buckley Field east of Denver. There is little or no irrigation nearby and the ground cover is mostly high plains grass and sagebrush. This lack of ground level moisture may account for the June to July drop in measured C_n^2 . If this is true, it is likely that values of C_n^2 in more humid regions, such as the central and eastern United States, are considerably greater than the measurements presented here.

A second surprising feature of Figure 3.2 is the difference between the measurements of March 1977 and February 1978. Normally, one would not expect them to be greatly different. However the winters of 76-77 and 77-78 were drastically different. In Colorado, the winter of 76-77 was unusually mild whereas 77-78 was more normal and had much colder temperatures. The warmer winter resulted in higher C_n^2 values than normal and this is shown in our measurements.

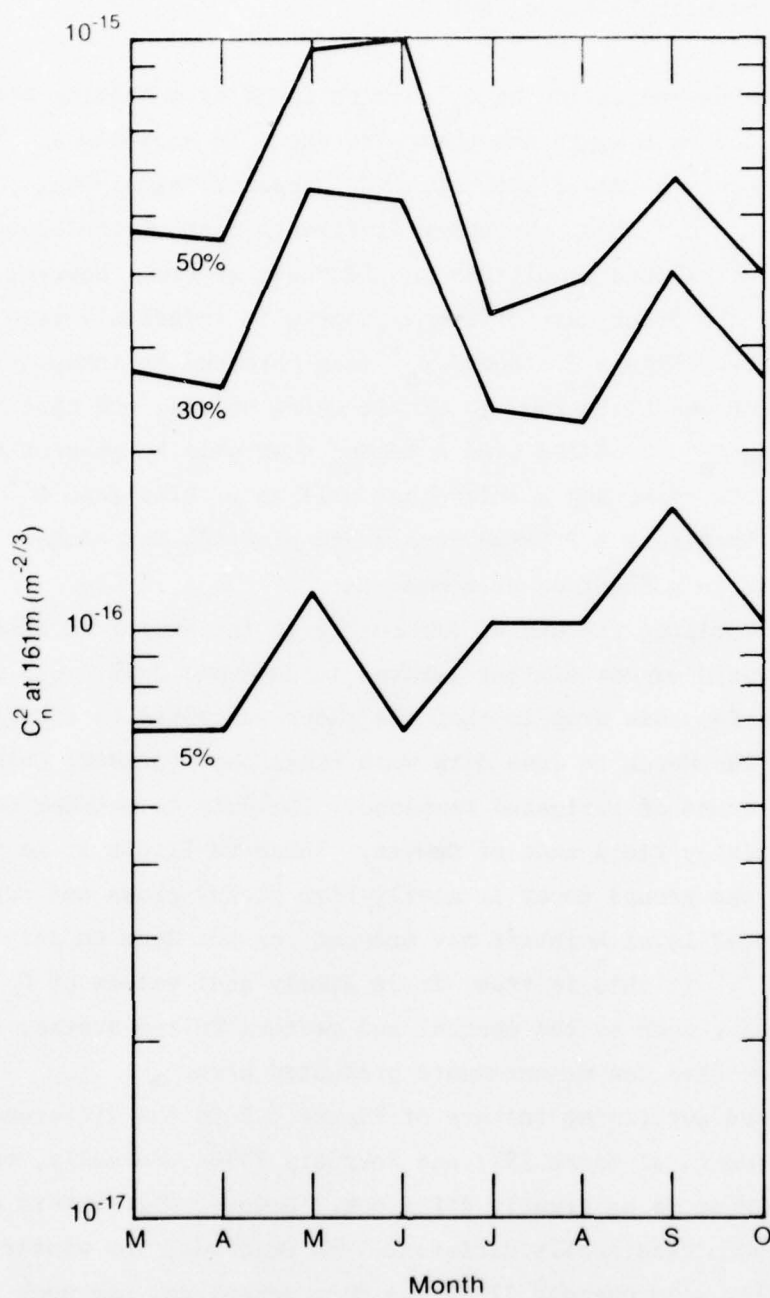


Figure 3.2(a). Monthly C_n^2 data at 161 m. Graphs show C_n^2 value that was greater than observed C_n^2 for that percentage of time.

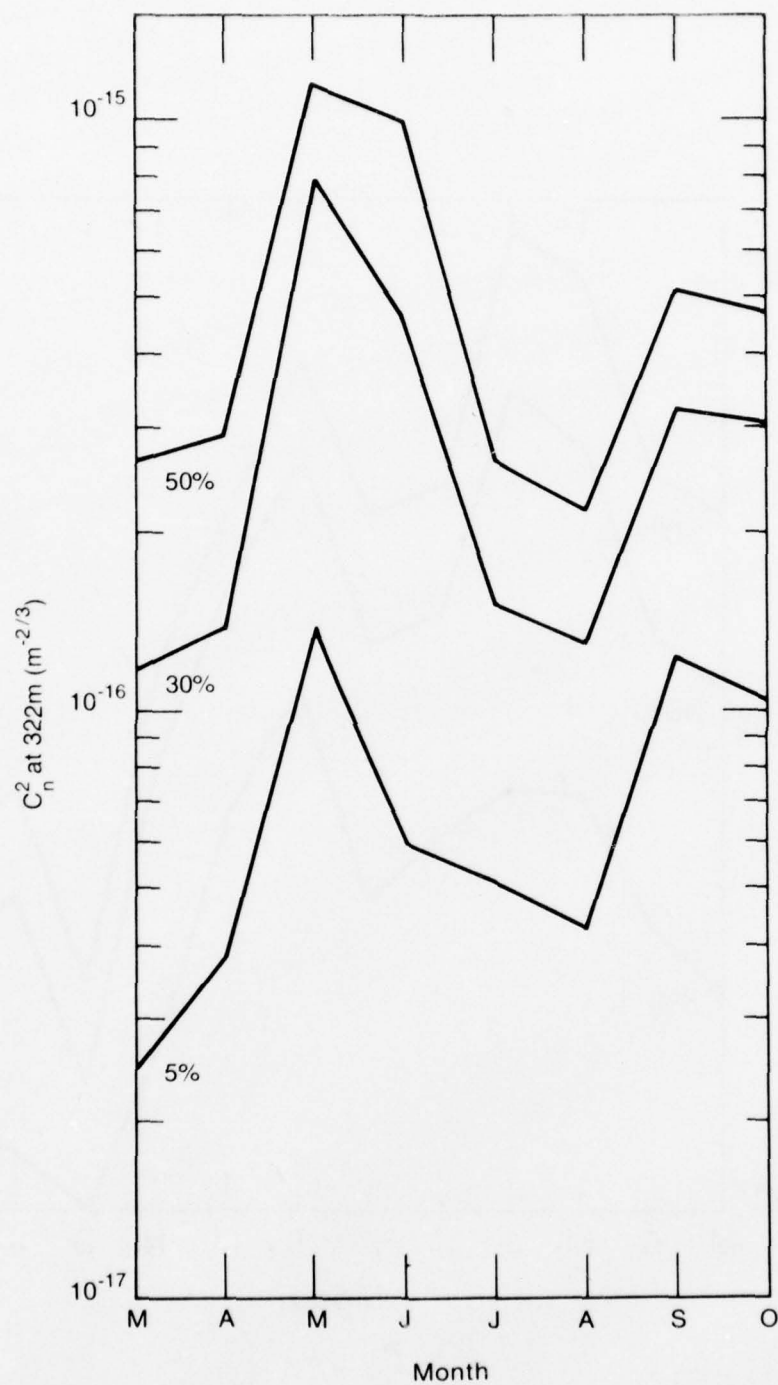


Figure 3.2(b). Monthly C_n^2 data at 322 m.

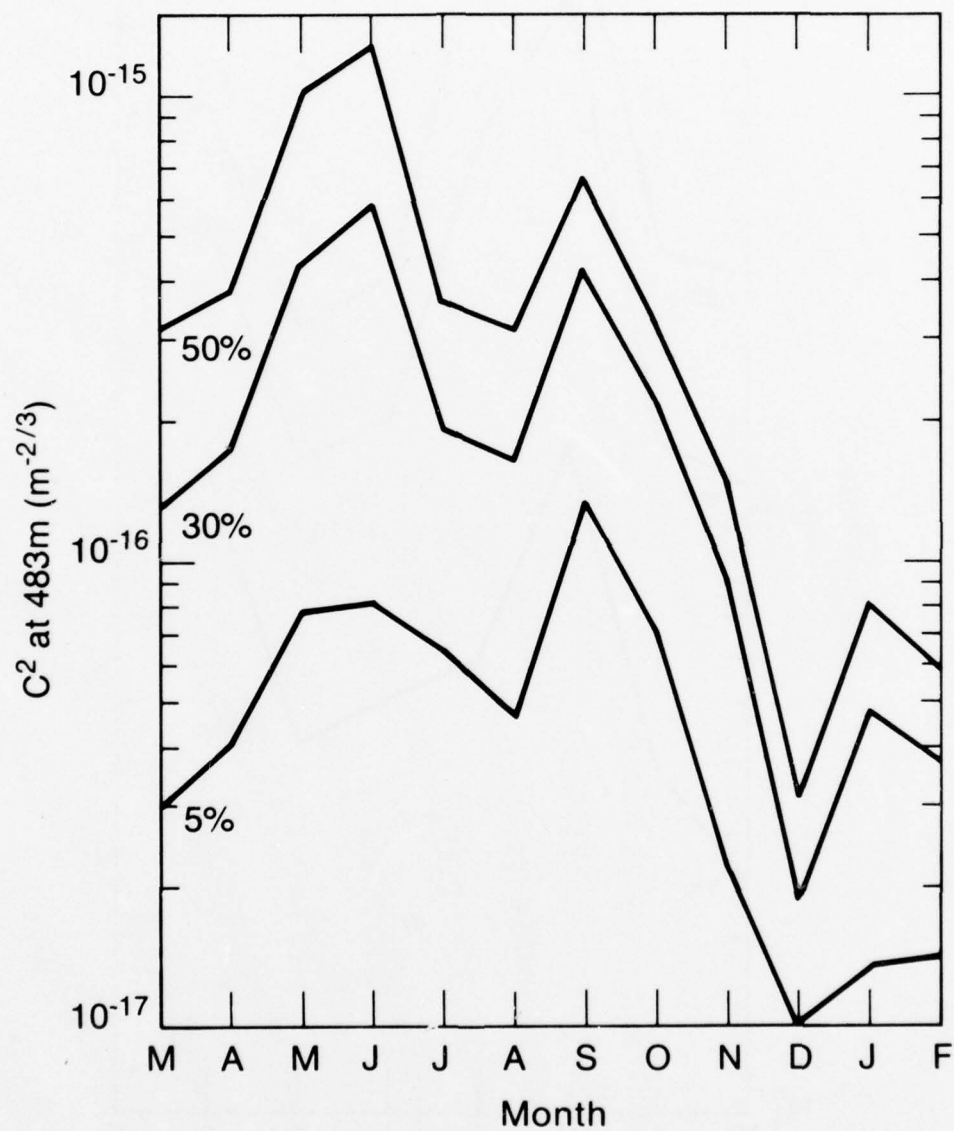


Figure 3.2(c). Monthly C_n^2 data at 483 m.

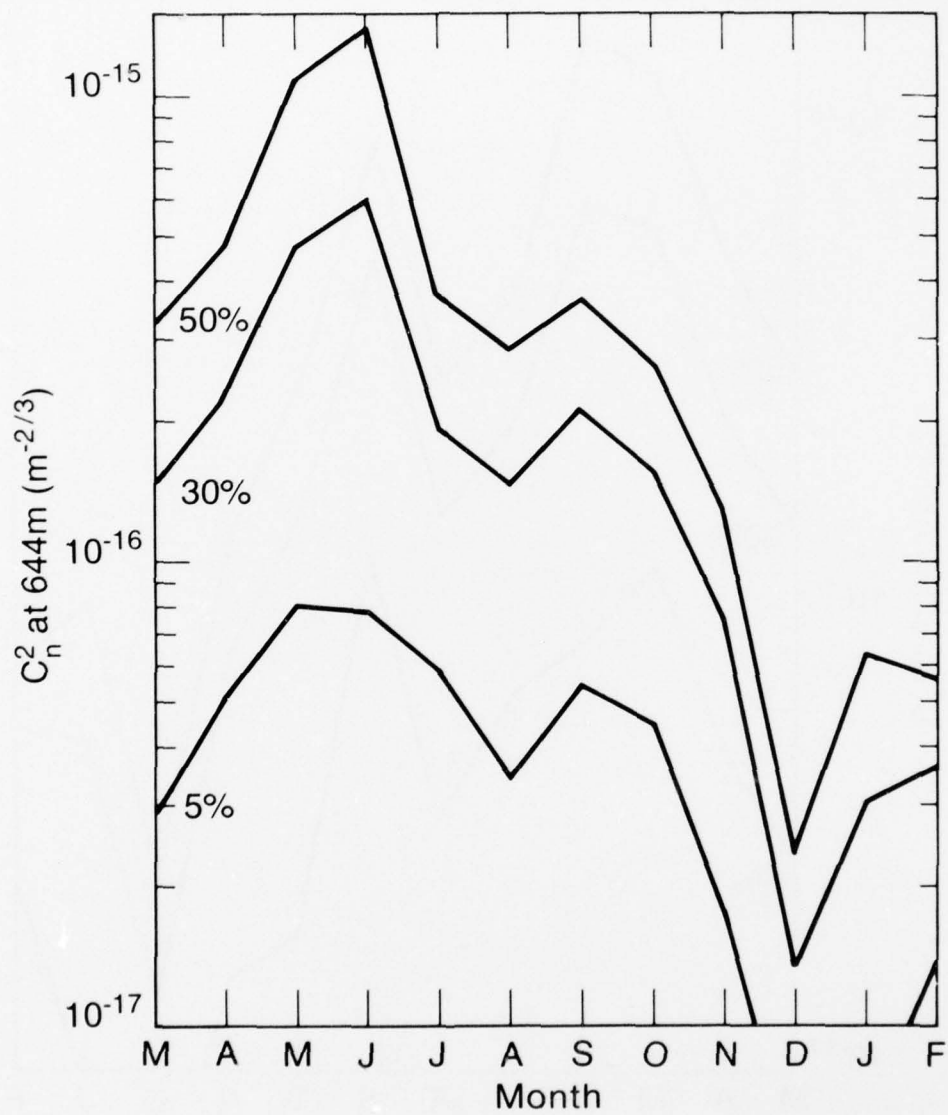


Figure 3.2(d). Monthly C_n^2 data at 644 m.

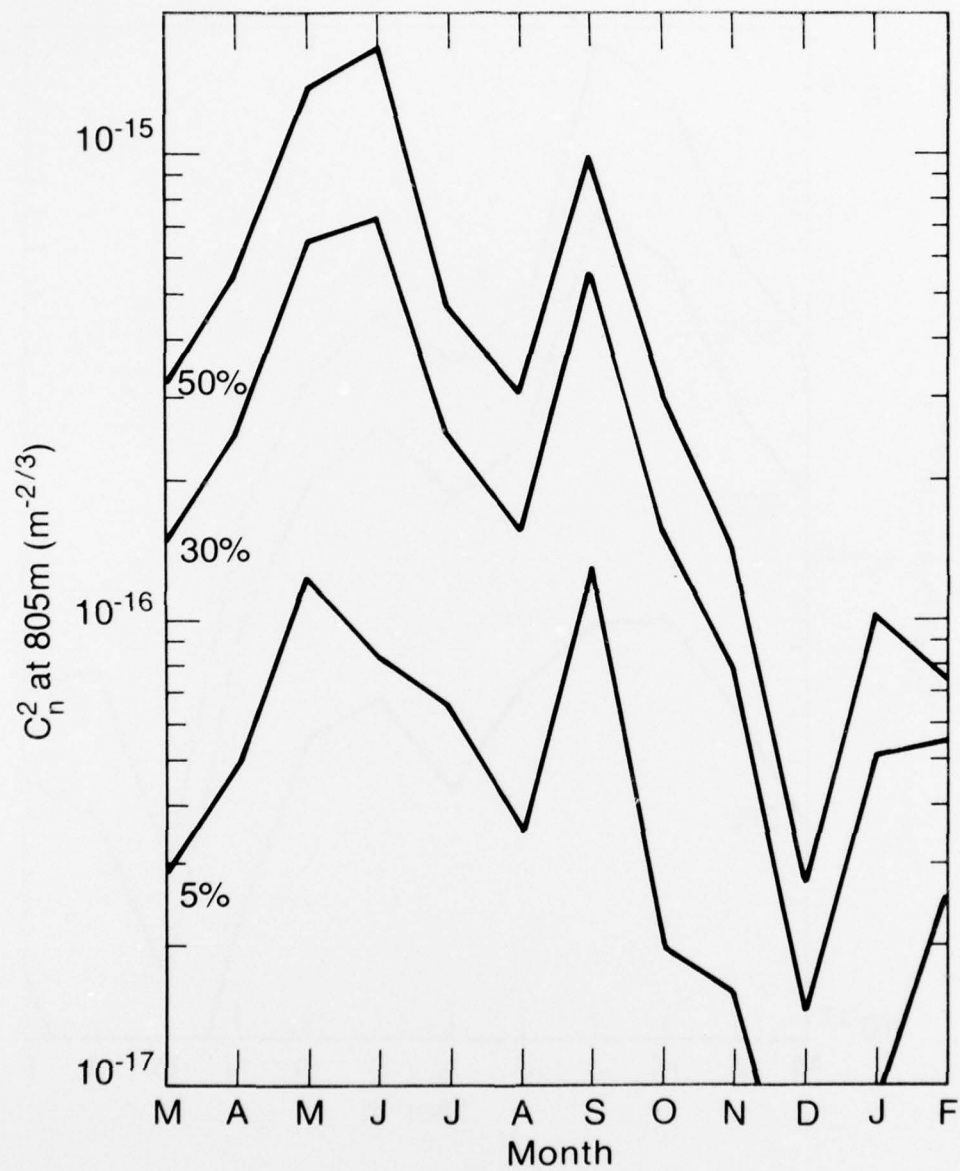


Figure 3.2(e). Monthly C_n^2 data at 805 m.

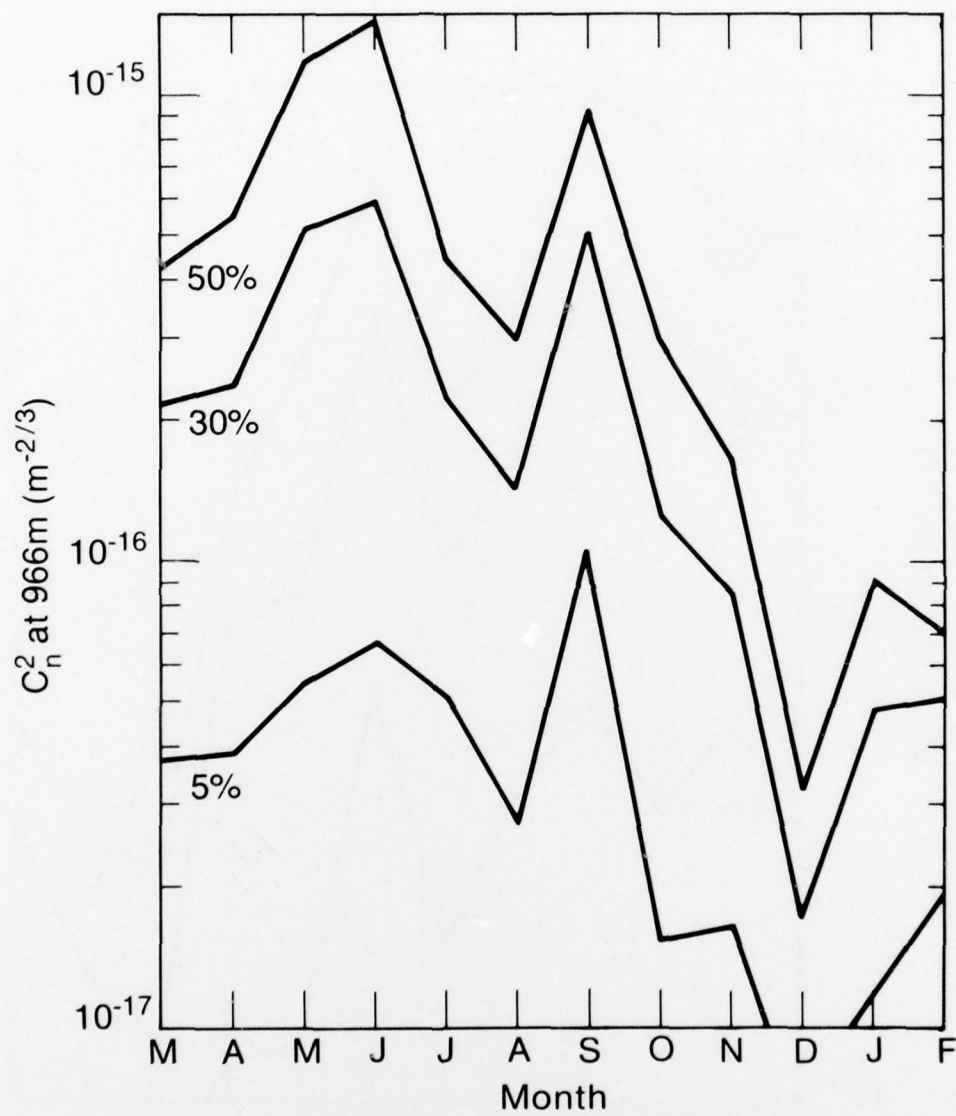


Figure 3.2(f). Monthly C_n^2 data at 966 m.

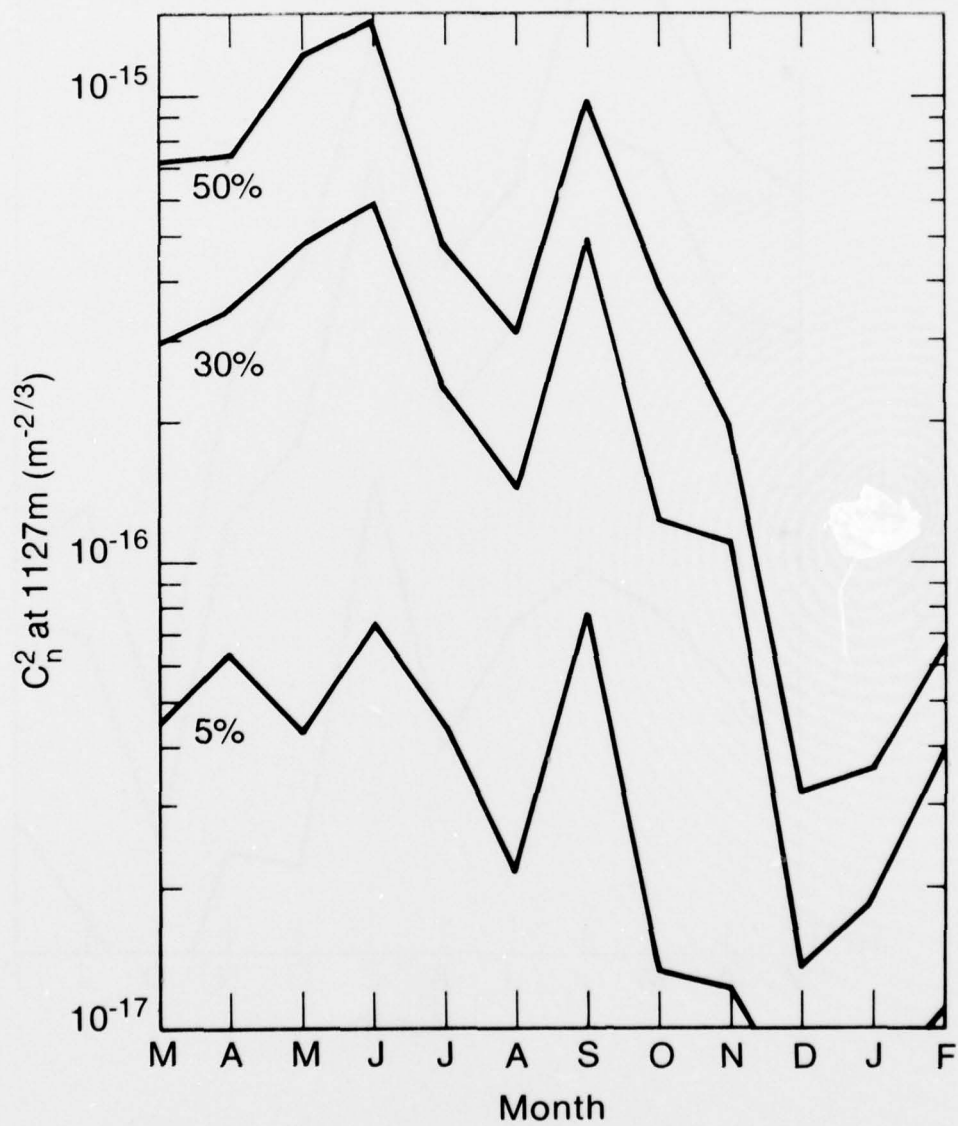


Figure 3.2(g). Monthly C_n^2 data at 1127 m.

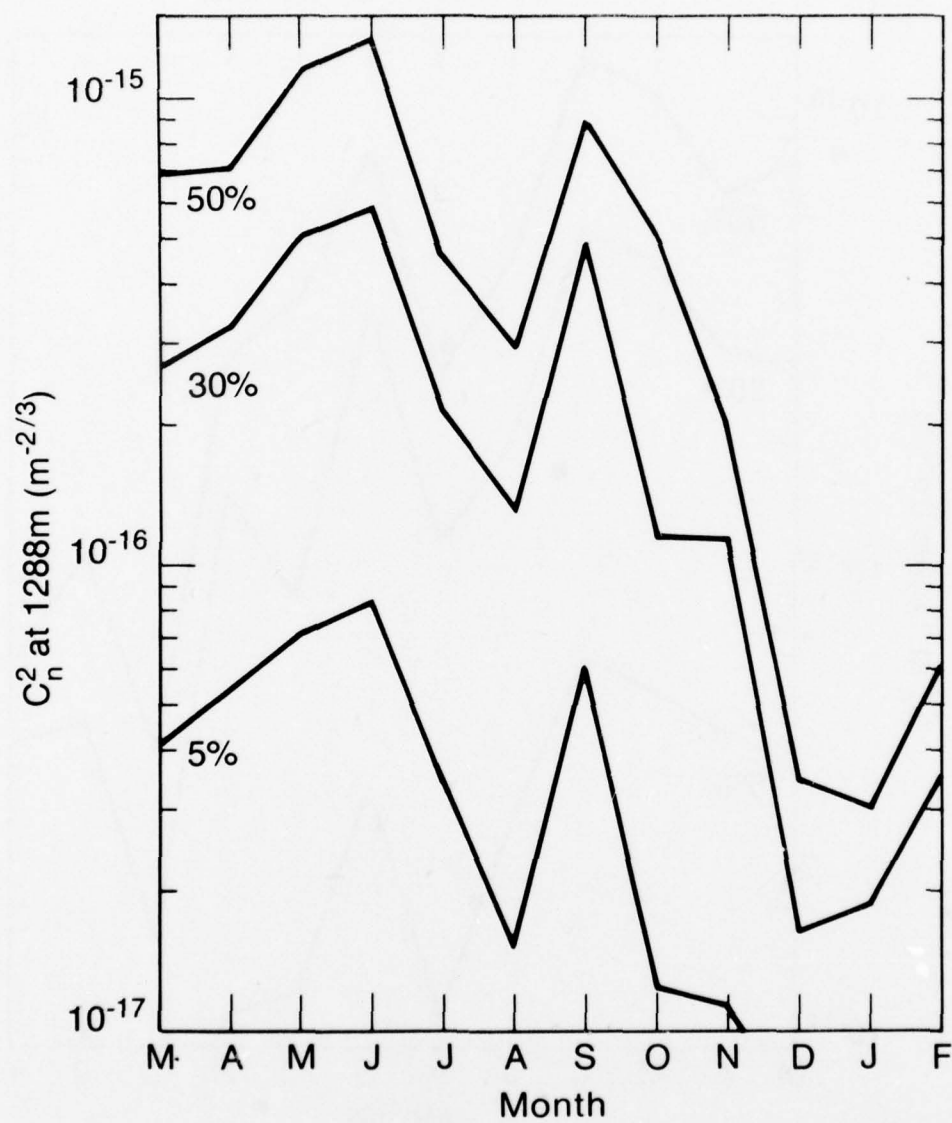


Figure 3.2(h). Monthly C_n^2 data at 1288 m.

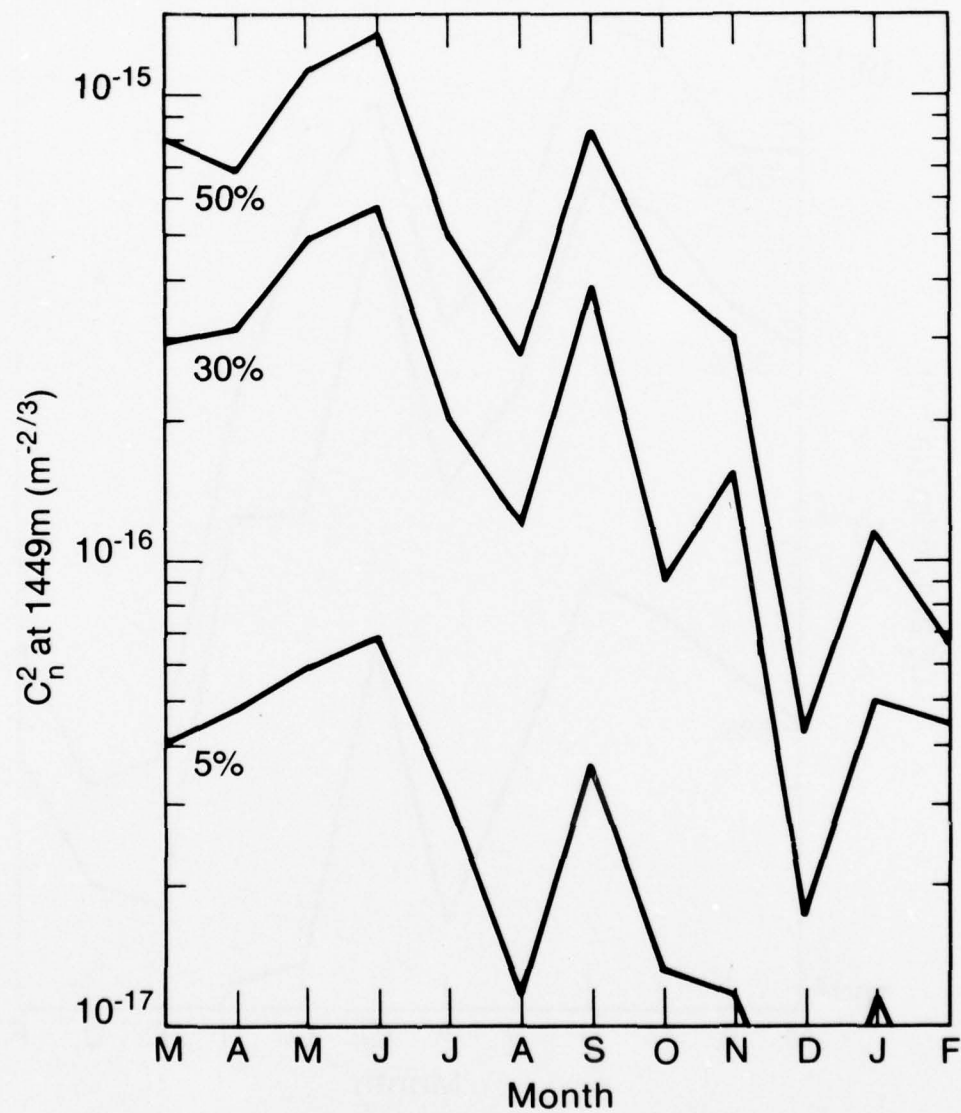


Figure 3.2(i). Monthly C_n^2 data at 1449 m.

TABLE 3.1. *Time Operated per Month*

Month	Minutes	Days
March	19260	20
April	26640	23
May	28140	22
June	17640	21
July	12060	11
August	14220	17
September	26160	22
October	3660	5
November	6540	5
December	7740	7
January	3960	4
February	3600	4

As one would expect, C_n^2 is significantly lower in the winter months. However, this should have little effect on an operational wind shear system, because hazardous wind shear generally does not occur in the winter.

The number of minutes operated each month is shown in Table 3.1. The total operating time was 2827 hr and covered 160 days.

3.4 Combined Hour-of-the-Day Histograms

The data can also be viewed on an hour-of-the-day basis for each range cell, but the results for just the 805 m range cell will be presented here. The histograms for each of the 24 hours in the day are shown in Appendix D. The 5%, 30% and 50% levels of these histograms are shown in Figure 3.3 which has two peaks in the C_n^2 values. The first peak occurs about midnight and the second at midday. These peaks are probably due to a combined effect of the temperature gradient and

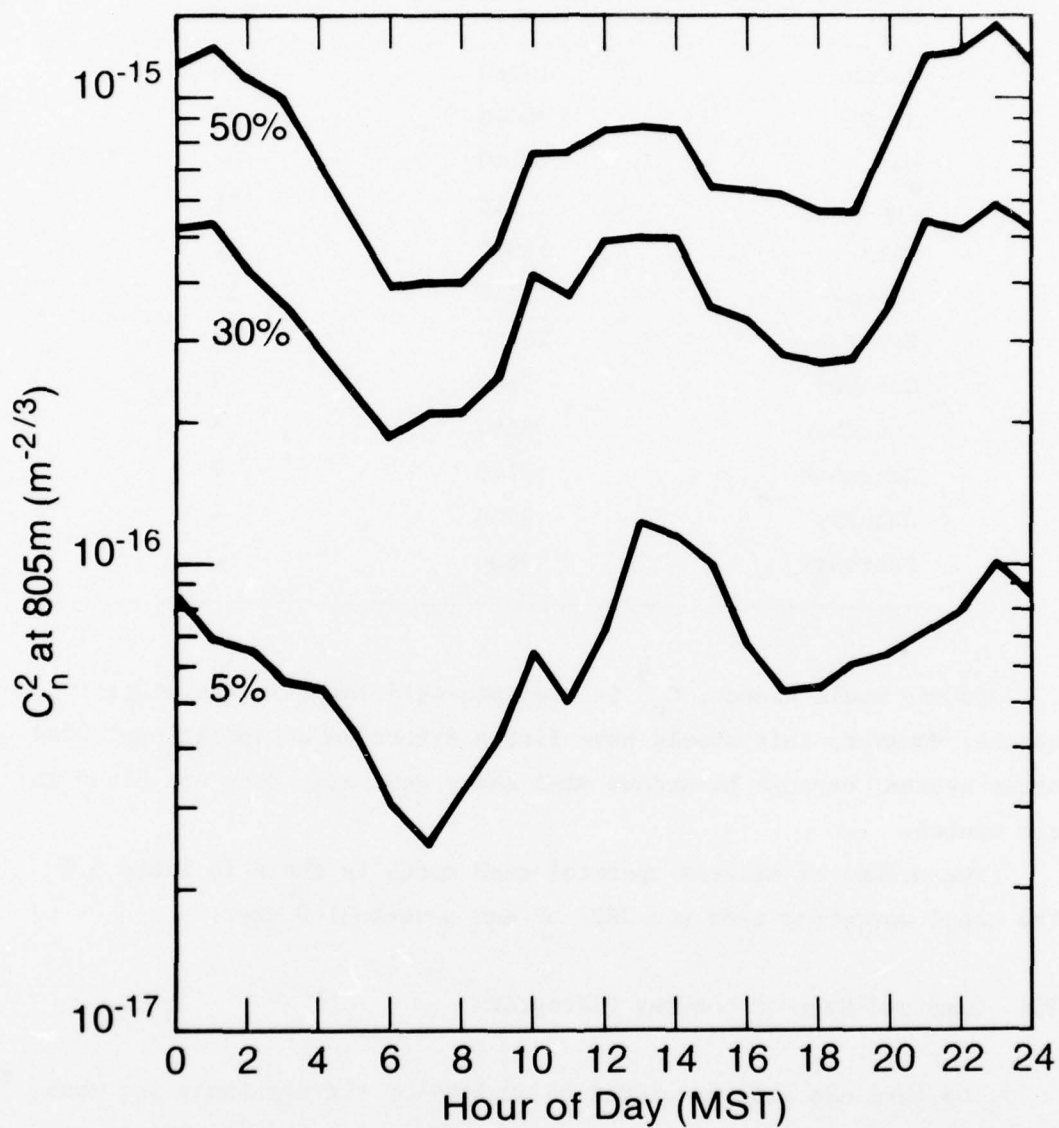


Figure 3.3. Hourly C_n^2 data at 805 m. Graphs show C_n^2 value that was greater than observed C_n^2 for that percentage of time.

mechanical turbulence. At sunrise there are large gradients, but very little turbulence. As the sun rises higher, solar heating and the resulting convection cause increased C_n^2 which reaches a peak shortly after noon. There is considerable convection, but very little departure from an adiabatic temperature gradient. Then the heating is decreased in the afternoon and the C_n^2 values decrease. As the ground cools in late afternoon and evening, the atmospheric stability increases and this causes large gradients. These large gradients require only small amounts of turbulence to cause large C_n^2 values, and C_n^2 reaches a peak about midnight. After midnight, the stability increases, but the turbulence dies out so that C_n^2 decreases to a minimum just before sunrise when the cycle starts over again.

So, the two peaks in Figure 3.3 are due to two different effects. The midnight peak is due to high stability, the resulting large gradients, and a small amount of turbulence. The noon peak is due to strong convection and small gradients. The minimum in C_n^2 at sunrise is due to a stable atmosphere (with large gradients) but very little turbulence.

3.5 Probability Law for C_n^2

An item of importance for system design is a general probability law for C_n^2 . Because large and small values of C_n^2 occur with some regularity, it is likely that C_n^2 does not follow a Gaussian distribution. A more suitable model for a parameter with a large variation is the lognormal distribution, i.e., $\log C_n^2$ being Gaussian. A straightforward way to check this is to plot $\log C_n^2$ on probability paper. If the plot is a straight line, then C_n^2 follows a lognormal distribution.

Figure 3.4 shows plots of $\log C_n^2$ at 805 m for each month data were taken. Figure 3.5 is a similar plot except the variable plotted is $\log C_n^2$ for every third hour of the diurnal cycle. Only the March to October data were used for Fig. 3.5. The conclusion from these two figures is that C_n^2 can be assumed to be lognormal. Further, since the

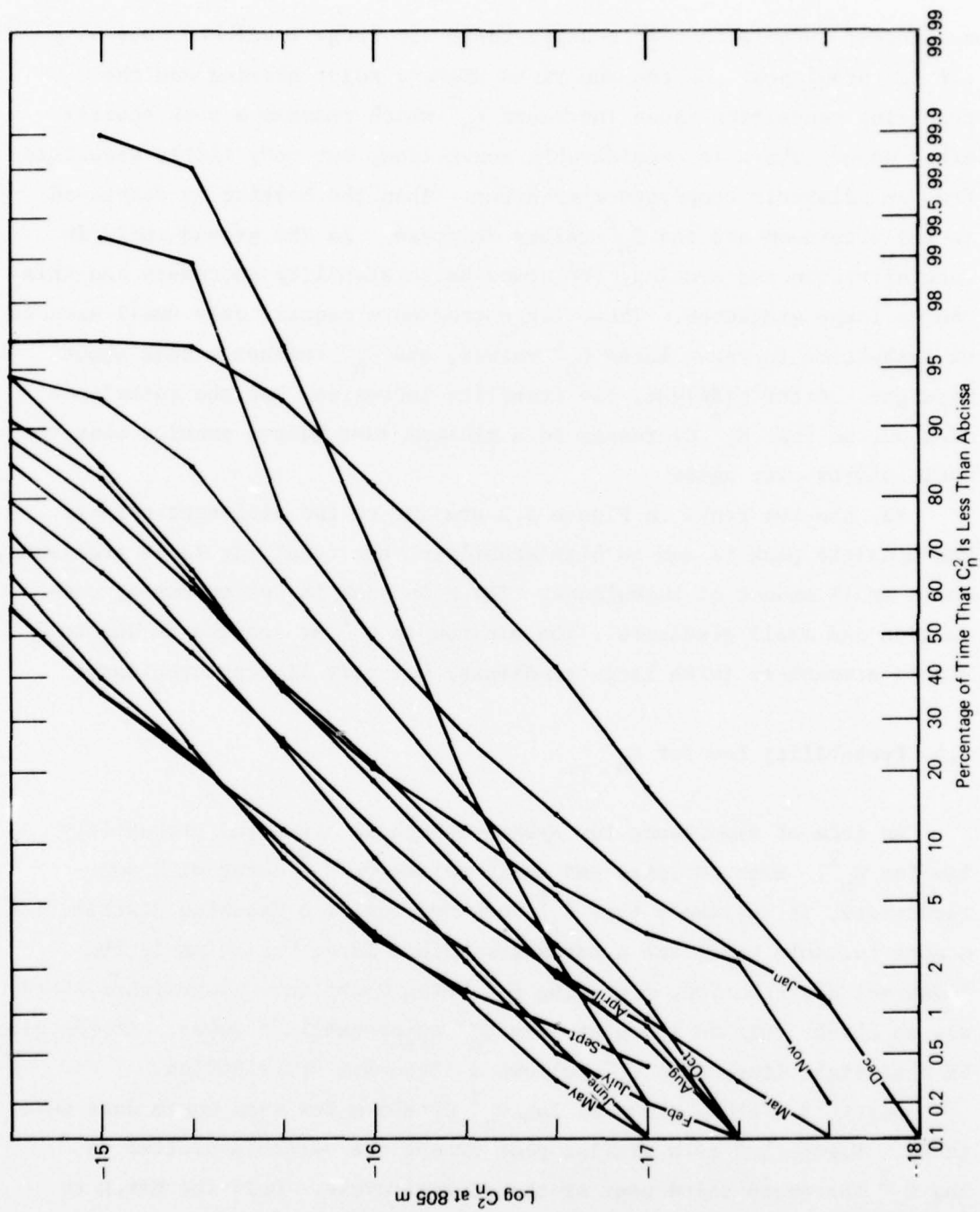


Figure 3.4. Probability distribution of monthly $\log C_n^2$ values.

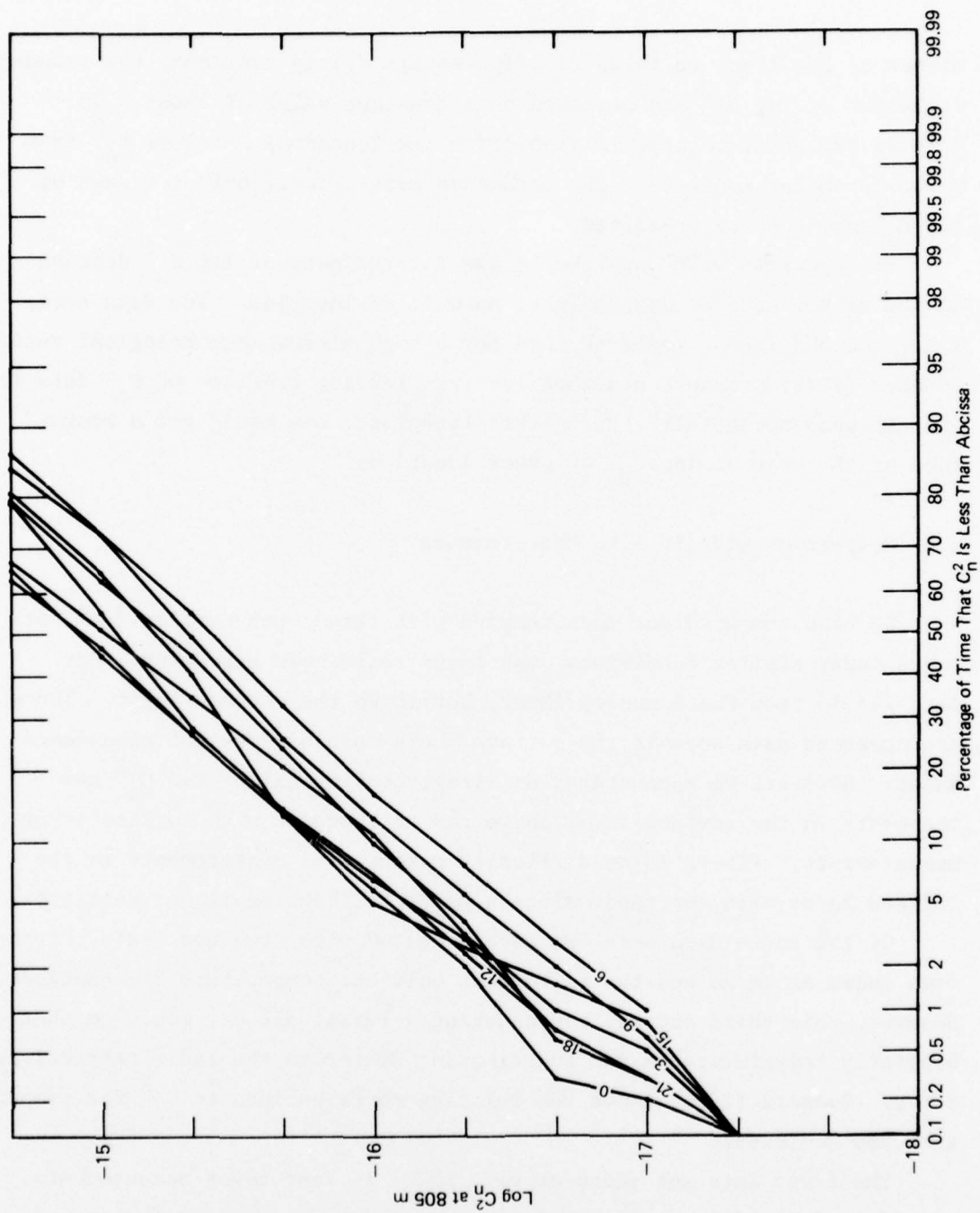


Figure 3.5. Probability distribution of certain hourly $\log C_n^2$ values.

slopes of the lines in these two figures are fairly constant, the standard deviation of $\log C_n^2$ can be taken as a constant value of about 6 dB.

This is important because it simplifies the lognormal model of C_n^2 from a two parameter model to a one parameter model, i.e., only the mean of $\log C_n^2$ needs to be specified.

The specific value one should use for the mean of $\log C_n^2$ depends on the month, hour of day, height, as well as location. The data here, i.e., the 50% lines, could be used for a high plains meteorological regime. Gossard (1976) presents a method for transferring profiles of C_n^2 data from one air mass to another. Using this technique, one could get a rough idea of the mean of $\log C_n^2$ at other locations.

3.6 Comparison with in-situ Measurements

We have compared our measurements with three much smaller data sets taken under similar conditions, and found reasonable agreement. Our data set is from the boundary layer, but above the surface layer. There are numerous data sets in the surface where models of height dependence exist. However, we encountered difficulty taking calibrated C_n^2 measurements in the surface layer so we can not compare with surface layer measurements. (There is no difficulty making wind measurements in the surface layer with our radar since a power calibration is not required.)

Of the three data sets, we have compared with, two use radio refractive index as we do and the third uses only the temperature fluctuations. However, this third one was taken during a relatively dry month so that hopefully temperature is the contributing factor to the radio refractive index. Gossard (1976) shows the relative contributions to C_n^2 for temperature and humidity.

The first data set (Bean et al., 1970) is four tower measurements of refractivity fluctuations using two microwave refractometers spaced 20 cm apart. The measurements were made in southeastern Colorado in October 1970. The height range is 75-130 m and the four measurements

range from 1.2×10^{-15} to $8.5 \times 10^{-14} \text{ m}^{-2/3}$. The measurements were taken when the refractometers were in regions with strong temperature gradients and so it is not surprising that they are 5 to 23 dB higher than our mean value for October at 161 m. Figure 2 of Bean et al. (1970) shows that the peak C_n^2 value in the region of strong temperature gradients is about 15 dB above a baseline. The conclusion here is that the agreement is reasonable.

The second data set (Gossard, 1976) is estimates of C_n^2 based on rawinsonde measurements and temperature fluctuation models. The relevant figure is 17 where the summer values are seen to be somewhat greater than $10^{-15} \text{ m}^{-2/3}$, while the winter values are somewhat less than $10^{-15} \text{ m}^{-2/3}$. Our values are less than this by 3 to 7 dB and since Gossard's data set is for Omaha, Oklahoma City, and Boston, the difference is not surprising.

The third data set (Ochs and Lawrence, 1972) is from temperature measurements made by aircraft in southeastern Colorado during November 1971. If the humidity was quite low, these measurements should not be greatly different than ours. The relevant figure is the average profile over land on page 36, where the C_n^2 range for heights above 160 m, is from 5×10^{-17} to 5×10^{-16} . This is in good agreement with our values for the month of November.

The agreement between our data set and these three others gives some confidence that our data is not drastically in error.

4. Operation at Low Elevation Angles

If any remote sensing shear detection system is to be effective, it must detect hazardous shear near the region where the aircraft is the most vulnerable, i.e., the glidepath. The spatial structure of meteorological phenomena that resulted in hazardous wind shear on two occasions has been studied by Fujita and Caracena (1977). They found that the hazardous region can be as small as a few km wide and that this hazardous region moves horizontally very fast. Thus, it is clear that a

shear detection radar must be capable of continually monitoring the wind at a fairly low elevation angle. Further, the radar must be capable of measuring winds at close ranges because the hazardous shear region may be positioned over the runway. This combination of operation at low elevation angles and close ranges is difficult for most radars. A comparison of the difficulty for a pulse and CW radar is discussed in Appendix C. This section will discuss these difficulties and some possible solutions for the FM-CW radar. Also, a way of displaying radial shear by means of a Plan Shear Indicator (PSI) is discussed and examples of clear air PSI displays are given. It is clear that low elevation angle PSI displays from the center of the runway to a range of 5 km would have provided adequate information to avert the two wind shear caused crashes studied by Fujita and Caracena (1977).

4.1 Plan Shear Indicator (PSI) Display

The PSI display is a qualitative display of wind shear first proposed by Armstrong and Donaldson (1969). It operates like a conventional PPI in that one can readily tell the azimuth angle and range to an area of significant shear. The velocity spectra for increasing ranges are arranged side-by-side and then used to intensity modulate a PPI oscilloscope at the current antenna azimuth angle. Then the antenna is moved and the process repeated. If the only return is from stationary targets, the PSI is a set of arcs of concentric circles and the intensity of the arcs is proportional to the received power from that range. If the targets are moving, they are offset from the arcs and the offset is proportional to the velocity. A change in velocity from one range cell to the next (wind shear if the targets are clear air) is then quite apparent because the spectra do not have the same spacing as the ground clutter.

A pulse-Doppler radar requires special signal processing to produce a PSI; however, the output of the FM-CW radar is already in the required format for a PSI without additional processing. Appendix A is a simplified

explanation of FM-CW Doppler processing and it shows that the spectra occur naturally in a range-ordered side-by-side fashion. So, to produce a PSI display, all that is required is to synchronize the output of the spectrum analyzer to a PPI type display. The PSI displays shown here were obtained in real time without a computer.

Figure 4.1(a) shows the output of the spectrum analyzer for a summer day with fairly high winds. The narrow markers show the location of the zero velocity points (ZVP), and the wider peaks are the clear air velocity spectra. The range cell size is 160 m, the maximum unambiguous velocity is 8.7 m/s, and the elevation angle is about 50°. In Fig. 4.1(a), the closest range cell is to the left and the farthest is to the right. An incoming velocity displaces to the left of the ZVP and an outgoing velocity displaces to the right. Figure 4.1(b) is a PSI display taken under the same conditions. The azimuth scan rate is about 1°/sec. It is immediately obvious that the wind is blowing from the lower left to the upper right. At the lower part of the PSI, the return is saturated, perhaps because of an aircraft. Along the left edge of the PSI, the second and third range cells have double peaked spectra. The double peaked spectra imply two regions in the same range cell with different velocities. This would imply strong wind shear, but this is not the type of situation one would expect to be hazardous. However, there would probably be considerable mechanical turbulence in the region of the 3rd through 6th range cells along the left side of the region covered in Fig. 4.1(b).

The maximum azimuthal scan rate for our radar is 3°/sec, and when the antenna is rotating at this rate the averaging time must be reduced so the result is not smeared. Figure 4.2 shows two PSI displays taken at a scan rate of 3°/sec with only a 50 ms averaging time as compared with about 3s averaging time for Fig. 4.1. Again the elevation is about 50°. Figures 4.1 and 4.2 were taken on different days.

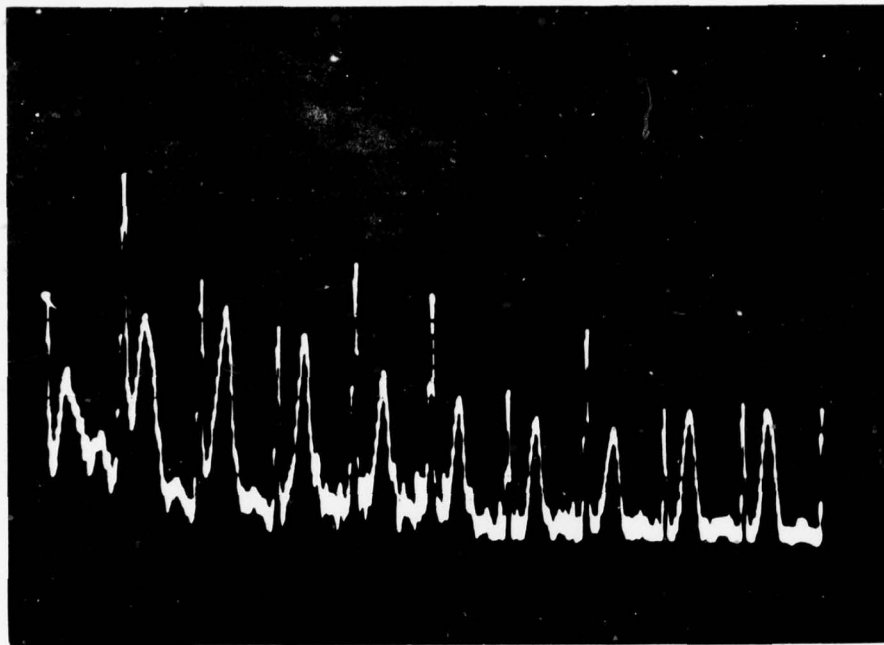


Figure 4.1(a). A-scope radar output.

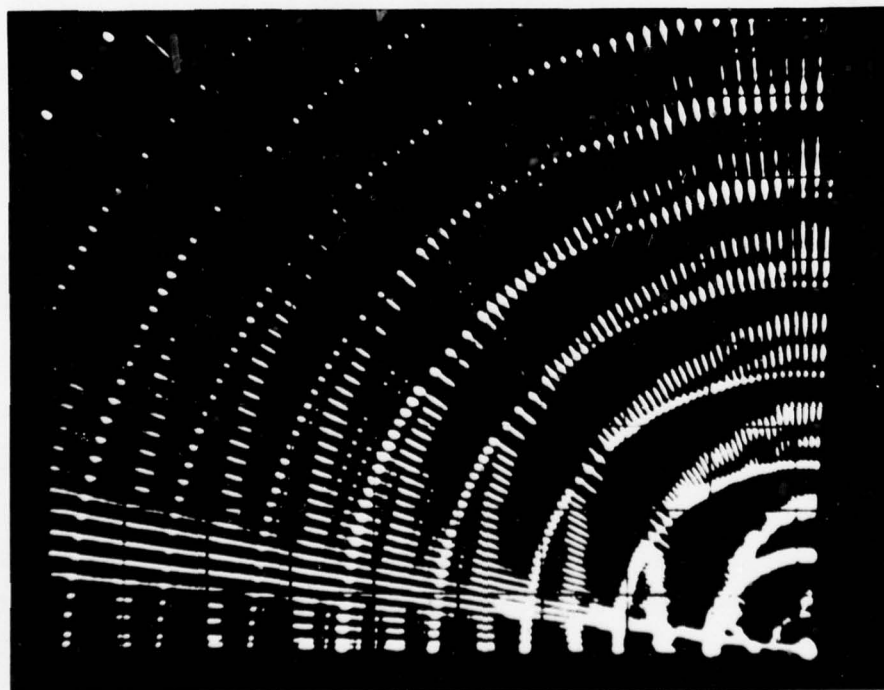


Figure 4.1(b). Plan Shear Indicator (PSI) display.

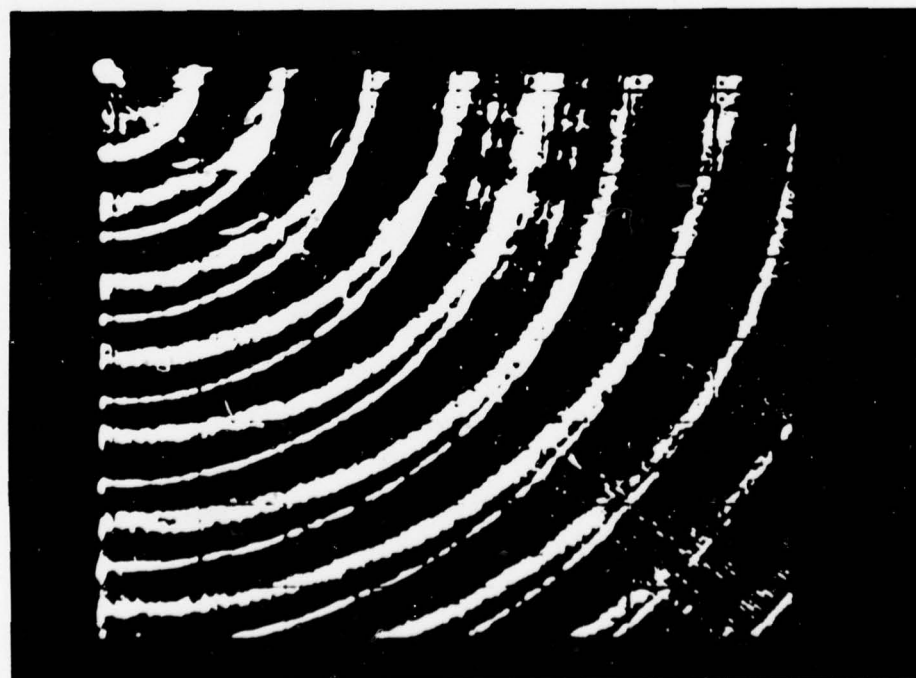


Figure 4.2. PSI displays.

Figure 4.3 is a relatively low elevation angle PSI taken alongside the runway at Buckley Field. The elevation angle of 29° is about the minimum we could achieve without removing the ground clutter. The range cell of 353 and maximum range of about 2800 m are the horizontal distances, but the 8 m/s represents a radial velocity. The radial lines that are white all the way out are due to signal processor saturation by aircraft or ground clutter. At a horizontal range of 2800 m and an elevation angle of 29° , the height being probed is about 1550 m. The region being probed gets higher as the range increases and eventually is above the top of the boundary layer. Because of the drier air, the return is less from above the boundary layer. At lower elevation angles the maximum range should increase. So, the problem with achieving ranges of 5 km is not sensitivity, but rather the capability to operate at low elevation angles.

A PSI type of display can give a very clear picture of radial winds along the glide slope if the problem of saturation by ground clutter can be solved. This is covered in the next section.

4.2 Ground Clutter Suppressors

As pointed out above, operation at elevation angles near the glide slope is highly desirable. However, the ground clutter then becomes large and saturates the signal processor. It is important to distinguish between two types of saturation, receiver saturation and signal processor saturation. Receiver saturation occurs when the return RF signal exceeds the dynamic range of either the RF amplifier or the mixer. Whenever ground clutter causes this type of saturation, wind measurements are not possible. The approach to this problem would be to use antennas with lower sidelobes. The second type of saturation occurs when the ground clutter return saturates the spectrum analyzer. Again, wind measurements are not possible when the spectrum analyzer is saturated. However, this large return is due to ground clutter and hence repeats

FM-CW Clear Air PSI

Buckley Field

6 Aug 1977

Elevation angle = 29°

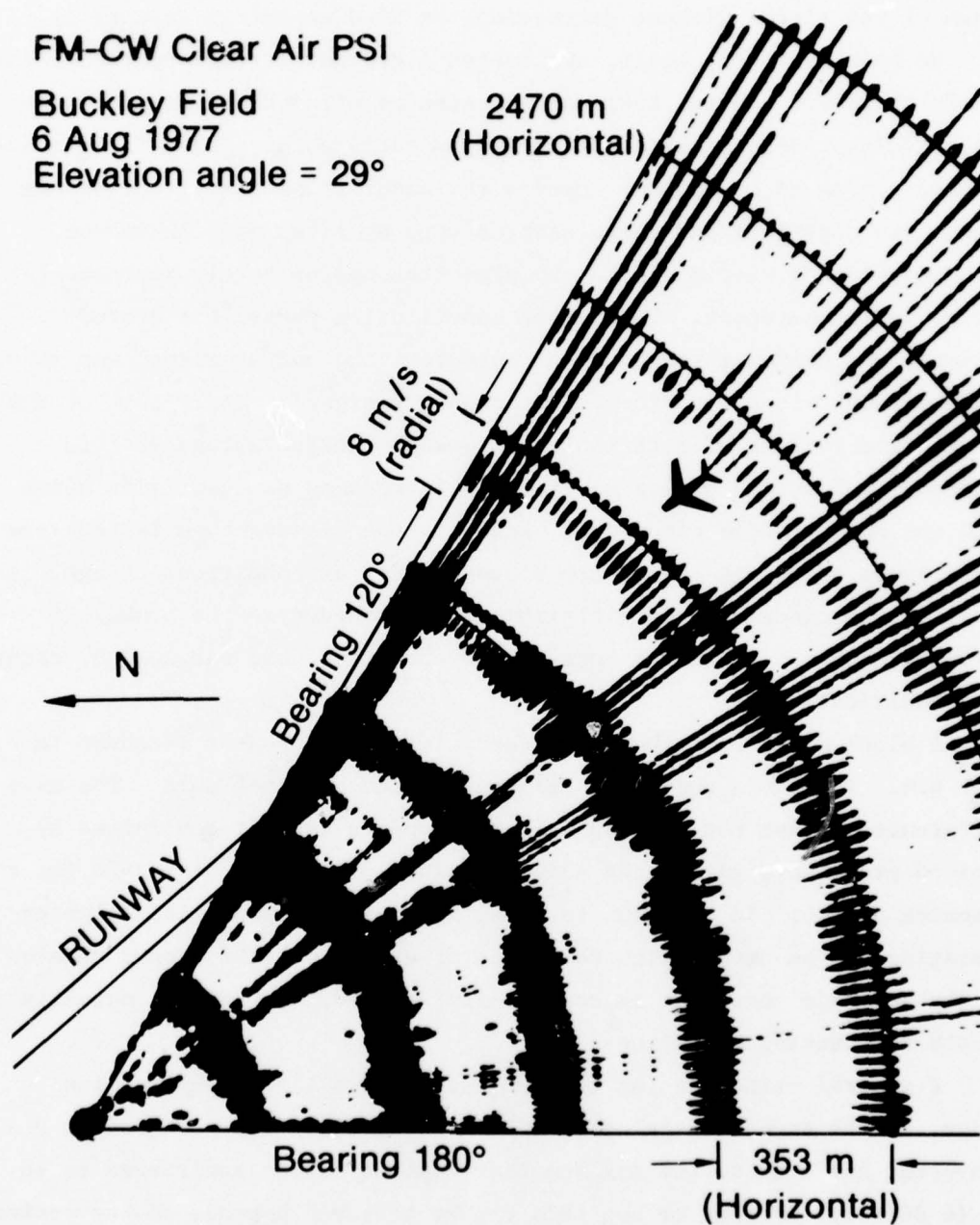


Figure 4.3. PSI display taken at Buckley Field. Elevation angle is 29° .

from one sweep to the next. A properly designed ground clutter suppressor can then eliminate the periodic component and greatly reduce the dynamic range of the signal without decreasing the wind measuring capability.

We have designed, built, and tested a ground clutter suppressor for the FM-CW radar. On the basis of experiences with the first model, we are building a second unit that should be satisfactory. The first model had two phases of operation. During the acquisition phase, the analog signal was digitized and these samples were averaged over 16 sweeps. This sequence of stored digital samples then approximately represented the periodic component. During the cancellation phase, the stored sequence was passed through a D-A converter; the output signal was smoothed and then subtracted from the incoming analog signal. The result of the subtraction is free of a periodic component. The advantage of this approach is that the analog subtraction introduces no quantizing noise into the non-periodic component. However, the disadvantage is that the unit cannot adapt and change the stored signal as conditions change. Also, it was clear that more flexibility was needed in the number of sweeps averaged. We felt a redesign of the first unit was needed, rather than modification.

A block diagram of the redesigned clutter suppressor is shown in Fig. 4.4. The basic concept is similar to the original unit. The main difference is that now the averaging and update rate is controlled by a micro-processor, giving the added flexibility that is desirable for a research device. In addition to block averaging, exponential weighted averaging can be used. With this type of averaging, the stored version of the periodic component is continually updated, so the unit actually adapts to changing conditions.

A general criterion for clutter suppressors is the suppression range, or the amount the clutter will be reduced. Since the output D/A converter has 8 bits, the maximum that clutter can be suppressed is 48 dB (6 dB/bit). Whether or not this can be achieved depends on the periodicity of the clutter signal. The experimental work with the first clutter

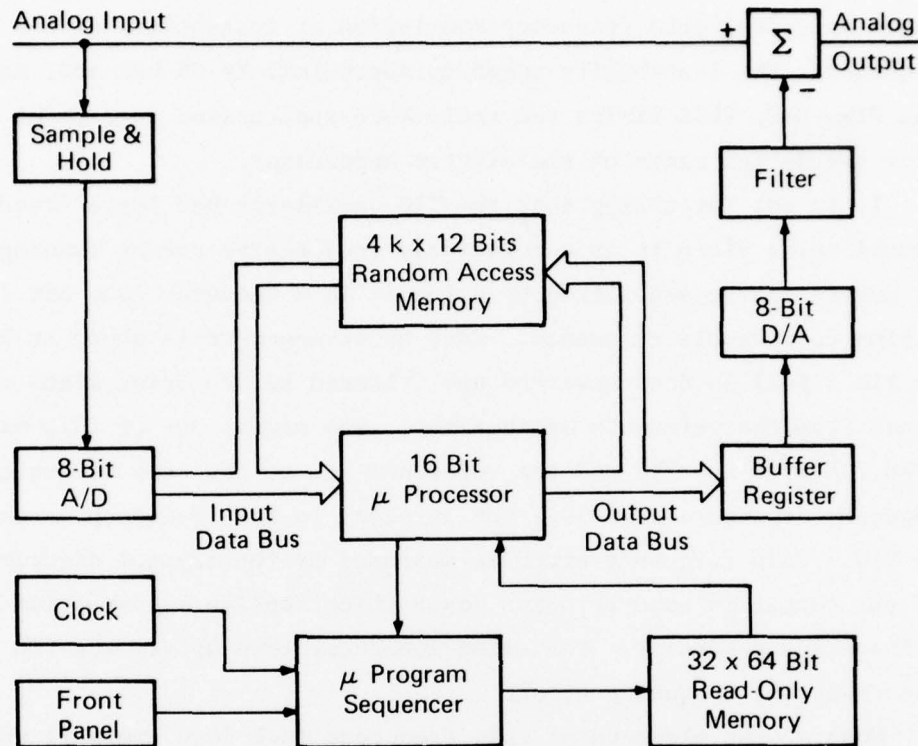


Figure 4.4. Ground clutter suppressor.

suppressor showed clearly that the clutter signal was not as periodic as had been assumed. The cause of the non-periodicity was traced to an RF instability, the elimination of which is discussed in the next section.

4.3 Sweep Frequency Stabilizer

An instability in the frequency sweep of an FM-CW radar lowers the potential clutter suppression. This is analyzed in Appendix B, and from Fig. B-2 the frequency stability required to achieve a given clutter suppression level can be determined. The signal source used in the FM-CW radar is an yttrium-iron-garnet (YIG) transistor oscillator modulated by a sweep generator. Noise in the driving stage of the YIG oscillator

causes an undesirable frequency modulation or instability of the output frequency. The instability range is approximately 35 kHz and, as seen from Fig. B-2, this limits the achievable suppression to a point well below the design range of the clutter suppressor.

It is not surprising that the YIG oscillator has large frequency instabilities since it is a relatively inexpensive source running open-loop. The source can be stabilized by using it in a feedback loop and frequency locking to a stable reference. Such an arrangement is shown in Fig. 4.5. The YIG signal is downconverted and filtered before being mixed with the signal from the reference synthesizer. The signal out of this mixer is at 10.7 MHz if the YIG and the reference are at the same frequency. The frequency departure from 10.7 MHz is equal to the frequency error of the YIG. This frequency error is measured by the crystal discriminator, and the output is used to drive logic which applies a correction signal to the sweep generator. The sweep generator then drives the YIG so as to correct the frequency error.

Most of the elements of this frequency lock loop are well understood. Only the stable reference synthesizer requires explanation. Commercial frequency synthesizers that use direct digital synthesis are available. However, there is none that could be programmed to run at the rates required here. So we designed such a unit. This is probably the first direct digital synthesizer specifically designed as a linear frequency sweeper. A block diagram of the design is shown in Fig. 4.6 where most of the lines are actually digital buses. The numbers by the lines indicate the number of bits in that bus.

At the start of the sweep, the value in the start register is on the tri-state bus and goes through the summer to the frequency register. Then the contents of the sweep register are on the tri-state bus and remain there until the end of the sweep. This bus value is then added to the contents of the frequency register, and the results are stored in the frequency register. This continues until the contents of the frequency register exceeds the value in the end register. Then everything is

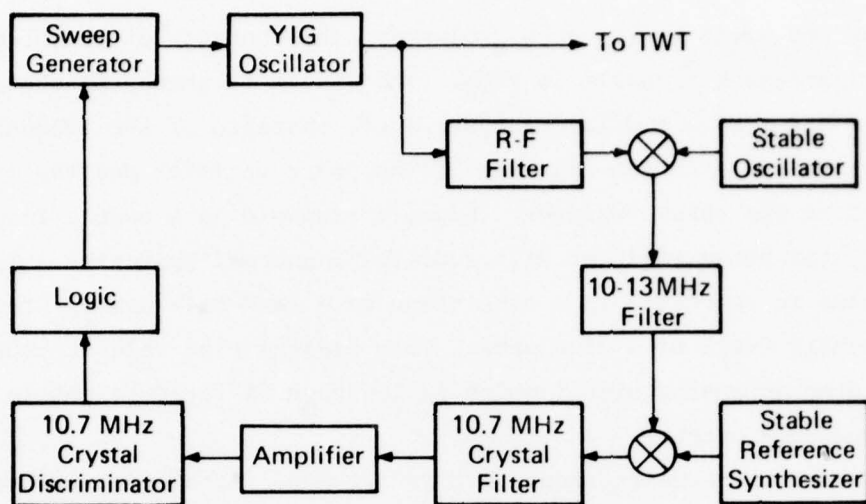


Figure 4.5. Frequency stabilization loop.

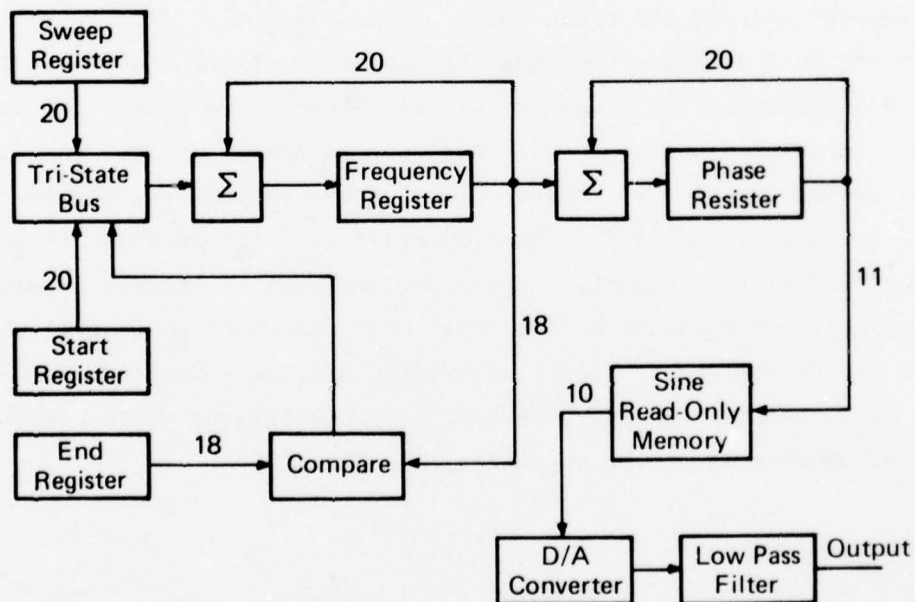


Figure 4.6. Swept reference synthesizer.

reset and the sweep starts over. Clearly, the contents of the frequency register increases linearly in time. The linear frequency is changed to quadratic phase by a similar process, i.e., contents of the frequency register are added to the contents of the phase register and the result is stored in the phase register. Since a sinusoid is a modulo function of phase, the phase register will overflow in normal operation. This phase value is converted to a sine value by a read-only memory programmed with one-half cycle of a sine wave. This digital sine value is then converted to an analog signal which is low-pass filtered to obtain the swept frequency output.

The output frequency range is 0 to 2.1 MHz. At a sweep rate of 0.67 MHz/ms, the frequency step size is 80 Hz. The basic clock rate is 2^{23} Hz or 8.388608 MHz and the main advantage of direct digital synthesis is that the clock stability alone determines the stability of the synthesized waveform.

Three things will limit the stability of the transmitted signal. The first thing is the stability of the stable reference synthesizer which depends only on the clock rate. There will be no difficulty eliminating this problem. Second, the stability of the stable oscillator will add directly to the frequency jitter. However, a commercial unit has been identified which has the required stability. Third, the YIG oscillator must be tightly locked to the stable reference. Because of a lack of an analytic model for the YIG oscillator, the behavior of the frequency locked loop cannot be predicted and must be studied experimentally.

Any solid conclusions on low angle operation must wait until the clutter suppressor and frequency stabilizer have been completed and tested in the radar system. However, we hope to cancel ground clutter by 30 dB and operate at elevation angles less than 10° .

5. Other Activities

During the course of the experiment, certain other activities were carried forward on a small scale at a low priority. Two of these activities

were in areas that have direct application for low level remote sensing at airports: low-level temperature profile measurement and wake vortex detection. The third activity, remote operation over phone lines, is essential for any operational application. This section discusses these three activities.

5.1 Radio Acoustic Sounding System (RASS)

Acoustic signals propagate at a speed proportional to the square root of the absolute temperature of the air. So, if a Doppler radar can detect an electromagnetic signal reflected from an acoustic signal, the temperature of the medium can be determined from the measured Doppler frequency. This technique is called RASS and has been verified experimentally for radar wavelengths of 8 m (Marshall et al., 1972). Since this wavelength is 80 times the wavelength of the FM-CW radar, it was not known if the RASS technique would work using a 6 KHz acoustic source and the 10 cm radar.

Previous work using microwave frequencies had failed because of the large acoustic absorption at 6 KHz acoustic frequency (approximately 10 dB/100 m). Some unknowns were 1) the effect of sweeping the radar frequency; 2) the effects of temperature gradients and turbulence for these short wavelengths; 3) the effects of horizontal wind. All of these effects would reduce the sensitivity of the system, but it was hoped that the FM-CW radar would have sufficient sensitivity to make up for these losses. We conducted some field tests with an acoustic source adjacent to the radar antennas and both the acoustic beam and the radar beam directed vertically. We were able to track the acoustic pulse to about a 400 m height. There were large and fast fluctuations in the return signal strength. This was probably due to small scale turbulence destroying the focus of the acoustic signal. Another effect was that the return seemed to be very height dependent. This is probably because the horizontal

wind advects the acoustic signal away from the radar beam. Or it could also be that temperature gradients are changing the acoustic wavelength.

The RASS experiments lasted for three days and were designed only to demonstrate feasibility of the technique at 10 cm radio wavelengths. It was shown that it is not difficult to operate in a RASS mode to heights of 400 m. With some optimization, heights of 600 m should be possible. We have since analyzed the effects of radar frequency sweeping and temperature gradients. The main conclusions are that frequency sweeping causes only a small loss in sensitivity, but temperature gradients can cause a significant sensitivity loss. So a practical RASS system must be a method for matching radar and acoustic wavelengths at different heights. The main problem with RASS seems to be that horizontal winds blow the acoustic signal out of the radar beam. This problem could be solved by moving the acoustic source upwind and letting the acoustic signal advect into the radar beam.

The RASS work consisted of the three days of experiment and some analysis of the effects of wavelength changes. We demonstrated the feasibility of low-level temperature profile measurements when the horizontal wind is not too great. This may be useful for predicting the onset and dispersal of fog at airports.

5.2 Wake Vortex Detection

The Naval Oceanic Systems Command (NOSC) in San Diego has an FM-CW radar somewhat like ours but without Doppler processing capability. Some unpublished work reports that they placed their radar near a commercial airport and observed some very strong, unexplained echoes. They decided that one possible explanation was the echoes were associated with the wake vortices of the commercial jetliners. They repeated the experiments using a smaller Navy plane that could fly either by jet or prop, but could not detect any echoes associated with the wake vortex.

While our FM-CW radar was at Buckley Field, we arranged for some of the jet trainers to fly over the antennas at about 400 m height and at a speed of about 360 mph. We could see no evidence of returns associated with the wake vortex of any of the aircraft.

The positive results at San Diego were obtained with large aircraft either landing or taking off. The negative results we obtained and the negative results obtained at San Diego were with smaller military aircraft (prop and jet) in level flight. The explanation is probably that only the larger aircraft generate a wake vortex that lasts long enough to be detected by radar.

5.3 Radar Operation Over Phone Lines

The FM-CW radar is designed so that data recording and antenna pointing are controlled by computer. The computer is located in the radar trailer and access to the computer is through a standard keyboard in the trailer. The keyboard is connected to the computer by an RS-232 interface. So with a commercial modem for an RS-232 interface and a teletype designed for phone line operation, we should be able to control the radar over the phone lines.

We were unable to have a phone line installed until the radar was at Buckley Field. But then, with only a small amount of effort, we were able to operate over phone lines. So, by remote control we can measure transmitted power, point antennas, start and stop recording, monitor data being recorded, and measure wind and other moments of the spectra.

6. Conclusions

The conclusions we draw from the experience gained in this experiment relate to the radar operation and to the C_n^2 measurements. First, are conclusions relating to the radar and its capabilities.

- (1) Our basic design for the FM-CW Doppler radar is such that off-the-shelf components can be used to assemble a very reliable wind sensing radar. We have had problems with the power transmitter and the computer, and these problems have both been traced to excessive heat. The power transmitter is similar to an uplink satellite transmitter and the traveling-wave-tubes used in those applications can achieve five years of continuous operation. We believe that our radar can be designed to meet reliability requirements of an operational radar.
- (2) We can measure winds to heights of 2 km almost all of the time in the spring, summer, and early fall. In the late fall and winter we can measure winds to heights of 500 m almost all of the time. Further, the radar is an all-weather device that can operate in clear-air, fog, rain, or snow.
- (3) The ability to operate at ranges of 5 km along the glide path depends more on the clutter suppression capability of the radar than on its sensitivity. The radar, as now configured, is sensitive enough to see to ranges in excess of 5 km at glide-slope angles if the ground clutter does not saturate the signal processor.

Second are conclusions relating to C_n^2 .

- (4) C_n^2 can be considered as a single parameter lognormal random variable. Only the mean of $\log C_n^2$ (where $\log C_n^2 = 0$ implies $C_n^2 = 1 \text{ m}^{-2/3}$) need be specified. The standard deviation of $\log C_n^2$ is about 0.6.
- (5) As expected, the mean C_n^2 values are highest in the summer and lowest in the winter.

- (6) The atmospheric diurnal variations are such that C_n^2 is at a maximum in the early afternoon and at midnight. The minimum C_n^2 values are generally seen at sunrise.
- (7) Because of the low humidities in Colorado, the C_n^2 values for the central U.S. and east coast will be greater than those reported here.

7. References

- Fujita, T. T. and F. Caracena (1977), An Analysis of Three Weather-Related Aircraft Accidents, Bull. of AMS, Vol. 58, no. 11, p. 1164-1181.
- Ottersten, H. (1969), Radar Backscattering from the Turbulent Clear Atmosphere, Radio Science, Vol. 4, no. 12, p. 1251.
- Probert-Jones, J. R. (1962), The Radar Equation in Meteorology, Quart. J. Roy. Meteorol. Soc., Vol. 88, p. 485-495.
- Armstrong, G. M. and R. J. Donaldson, Jr. (1969), Plan Shear Indicator for Real-Time Doppler Radar Identification of Hazardous Storm Winds, J. Appl. Meteor., Vol. 8, p. 376-383.
- Marshall, J. M., A. M. Peterson, and A. A. Barnes, Jr. (1972), Combined Radar-Acoustic Sounding System, Applied Optics, Vol. 11, no. 1, p. 108-112.
- Bean, B. R., R. E. McGavin, R. B. Chadwick, and B. D. Warner (1971), Preliminary Results of Utilizing the High Resolution FM Radar as a Boundary-Layer Probe, Boundary-Layer Meteorology, Vol. 1, p. 466-473.
- Gossard, E. E. (1977), Refractive-Index Variance and its Height Variation Distribution in Different Air Masses, Radio Science, Vol. 12, no. 1 p. 89-105.
- Ochs, G. R. and R. S. Lawrence (1972), Temperature and C_n^2 Profiles Measured Over Land and Ocean to 3 km Above the Surface, NOAA Technical Report ERL 251-WPL22.

APPENDIX A.

A SIMPLIFIED EXPLANATION FOR PROCESSING OF FM-CW
DOPPLER RADAR SIGNALS FROM DISTRIBUTED TARGETS

R. B. Chadwick and R. G. Strauch
NOAA/ERL/Wave Propagation Laboratory
Boulder, Colorado 80302

ABSTRACT

The concept of FM-CW Doppler processing is explained by showing it to be a special case of a correlation receiver with a frequency offset reference. For a linear FM signal, time delay and frequency shift can be arranged to cancel each other, and this results in considerable simplification of the correlation receiver. The number of range cells and the number of frequency bins per range cell are shown to be related to the sampling obtainable by a digital spectrum analyzer.

This appendix is to be published in IEEE Trans. on Aerospace and Electronic Systems, January 1979.

A SIMPLIFIED EXPLANATION FOR PROCESSING OF FM-CW

DOPPLER RADAR SIGNALS FROM DISTRIBUTED TARGETS

R. B. Chadwick and R. G. Strauch
NOAA/ERL/Wave Propagation Laboratory
Boulder, Colorado 80302

I. INTRODUCTION

The simplicity and flexibility of FM-CW Doppler radar processing makes it an attractive technique. The use of this technique for over-the-horizon HF radars is discussed by Barrick (1973). Strauch et al. (1976) used the technique at S-band with an off-line digital Fast Fourier Transform (FFT) to measure Doppler shifts associated with returns from refractive-index inhomogeneities in the clear atmosphere. Chadwick et al. (1976) used a standard spectrum analyzer to measure these same Doppler shifts and showed the feasibility of real time wind measurements. The technique has always been difficult to explain because range and velocity information are extracted and separated simultaneously by a single spectrum analyzer or FFT. The purpose here is to give a simple explanation by showing that FM-CW Doppler processing is a special case of a correlation receiver. Also, the importance of the number of samples per sweep and the number of sweeps coherently processed will be pointed out.

A different way of explaining FM-CW Doppler processing is given by Strauch (1976).

II. CORRELATION RECEIVER

Suppose that a transmitted signal, $s(t)$ has an autocorrelation function $R_s(\tau)$ as shown in Fig. 1, and that this signal is used in a conventional correlator as in Fig. 2a. The range is determined by the reference delay τ , and the range resolution, Δ , is determined by the width of the autocorrelation function envelope. The number of cycles inside the envelope of the autocorrelation function is $2\Delta/\lambda$, which is generally in the range of 10^2 to 10^4 . When a target moves through the range cell at delay τ , the output of the integrator will trace out the autocorrelation function and the frequency of this signal will be the Doppler frequency associated with the target. A special case of this is the widely used police speed measuring radar where the transmitted signal and the autocorrelation function are sinusoids.

When measuring the velocity of moving targets with a correlation receiver, the necessary integration should be accomplished not with a low-pass filter, but with a bandpass filter, or equivalently a spectrum analyzer. The configuration shown in Fig. 2b will allow the measurement of velocity spectra associated with either point or distributed targets. However, velocity sense (incoming or outgoing) cannot be identified since only real signals are used. However, velocity sense can be obtained by introducing a frequency offset, f_o , into the reference; this is acceptable because the offset simply translates the spectrum. It makes no difference whether the frequency offset is on the receiver side or the reference

side of the correlator (or both) A correlation receiver with a frequency offset reference is shown in Fig. 2c. Zero velocity targets will now appear at f_0 and velocity sense can be determined by whether the return is above or below f_0 . This type of radar can measure range and velocity spectra of a distributed target regardless of the form of the transmitted signal. The performance of this type of radar when $s(t)$ is a completely random signal has been studied extensively and thoroughly verified experimentally by Cooper and McGillem (1967), Cooper, McGillem, and Waltman (1969), and applied to distributed targets by Chadwick and Cooper (1972).

A disadvantage of this type of radar is that the correlator must be timeshared (or parallel correlators must be used) to examine multiple range cells. A configuration using parallel correlators (one for each range cell) is shown in Fig. 3. The output of the spectrum analyzer of the i^{th} correlator is the velocity spectrum for the (point or distributed) target at a range determined by delay τ_i and this spectrum is centered at f_i . Up to this point, the form of $s(t)$ has not been specified. If $s(t)$ is a linear FM signal and if the values of f_i and τ_i are chosen correctly, Fig. 3 can be greatly simplified as shown below.

III. LINEAR FM SIGNALS AND DOPPLER PROCESSING

Three requirements on the parameters in Fig. 3 can greatly simplify the receiver structure. First, let $s(\tau)$ have constant amplitude and a linear frequency modulation as in Fig. 4. The solid line is the instantaneous

frequency of the transmitted signal and the dashed line is the instantaneous frequency of the received signal reflected from a point target at a range $c\tau/2$, where c is propagation velocity and τ is the round-trip delay time. Note that with a linear FM signal the delay function in the correlation receiver can be accomplished by a time delay or a frequency shift.

The second requirement is that the analyzers are gated off during the time intervals $(jT, jT+\tau)$, $j=0,1,2 \dots$. This effectively reduces the duty cycle so that the percentage loss of sensitivity is $100 \tau/T$. For certain meteorological targets, where delays are on the order of tens of microseconds and sweep lengths are on the order of milliseconds, this sensitivity loss is negligible.

The third requirement is that the frequency offset, f_i , for the i^{th} branch of the receiver be equal to i/T . Then the solid and dashed lines in Fig. 4 will be colinear, except at the start and end of the sweep for all received signals whose delay is i/B or whose range is $\frac{ci}{2B}$. So, during the time the analyzers are gated on, the signal at the output of the i^{th} frequency offset is just $s(t)$. The frequency offset is equal to the frequency shift corresponding to range or delay. This causes the first of two simplifications. Since, during the processing time, the frequency shifts due to the delay elements are the same as the frequency offsets, these frequency translations cancel so that all of the delay elements and frequency shift elements (in Fig. 3) can be removed. The second simplification then comes about because each of the parallel correlators has the same reference and received signals and so only one

correlator is necessary to simultaneously measure the velocity spectrum for each range cell. The parallel correlator structure of Fig. 3 therefore reduces to the structure in Fig. 5a. Because the frequency offsets are different for each delay, the spectrum of the correlator output is translated differently for each delay or range. Therefore, the output of the single spectrum analyzer has the spectra for each range cell displaced in frequency as in Fig. 5b.

The output can be visualized further by assuming that the return is from uniformly distributed, stationary ground clutter. Then the signal into the spectrum analyzer will be repeat exactly from one sweep to the next. This signal will then produce a discrete spectrum with components only at multiples of $1/T$ which are equal to f_i . The location of these discrete components in Fig. 5(b) are zero velocity points for the i^{th} range cell and are labelled ZVP_i . There is a requirement on the signal source to insure that a stationary return produces a discrete spectrum. The source must meet a frequency stability requirement. However, there is no requirement on the sweep-to-sweep phase of the signal. The sweeps do not have to be coherently generated.

Two additional points should be made: first, the velocity sense in the closest bin can not be determined. The reason for this is that the reference delay for the closest bin is zero and the frequency offset to cancel the delay is zero and without a frequency offset reference, sense can not be determined. If an FFT is used, the velocity sense in the last bin is also lost. This problem can however, be overcome by using a spectrum analyzer that oversamples and has an anti-aliasing filter.

Second, when the Doppler frequency becomes high enough, the return appears in the next higher or lower bin, i.e., it is ambiguous. However, even though this occurs, the frequency translation distance from a velocity spectrum to the zero velocity point with which it is associated is still the mean velocity at that range. The ambiguity function for this type of radar signal is discussed by Strauch and Chadwick (1976). The maximum unambiguous velocity is derived below.

IV. RANGE, VELOCITY, AND DISPLAY PARAMETERS

Before deriving expressions for maximum range, maximum unambiguous velocity, number of range cells per display, and number of Doppler frequency bins per range cell, it is necessary to make some assumptions about the spectrum analyzer. Although a fully analog analyzer could be used, a fully digital technique such as an FFT or a hybrid recirculating memory time compression spectrum analyzer allows synchronization of the sampling to the sweep, and this is desirable. Assume that the maximum frequency of the analyzer is f_m and δ is the frequency resolution (or the frequency per bin of the output display). So f_m/δ is the number of frequency bins per display. (It will be shown below that δ is the Doppler frequency resolution of the system.) Further, assume that the input to the spectrum analyzer is sampled N times for each sweep of the transmitted signal and that there are m sweeps coherently processed. Thus, the number of time samples required for a processing interval is Nm and these samples result in f_m/δ frequency bins in the output. The ratio of these two is characteristic of the spectrum analyzer. If

$$p = \frac{\text{no. of time samples}}{\text{no. of frequency bins}} = \frac{Nm\delta}{f_m},$$

an FFT analyzer with Nyquist sampling is characterized by $p = 2$. The particular commercial hybrid analyzer we use oversamples, requiring 1500 time samples for 500 frequency bins and thus for that analyzer, $p = 3$.

From Fig. 4, it is seen that the maximum range, r_m , is given by

$$r_m = \frac{cT}{2B} f_m = \Delta T f_m$$

where $\Delta = c/2B$ is the range resolution. Now T can be replaced by the number of samples per sweep multiplied by the sampling interval $1/pf_m$. Solving for the number of range cells per display, one obtains

$$\frac{r_m}{\Delta} = \frac{N}{p} \frac{\text{range cells}}{\text{display}} .$$

Also, it is seen that dividing the number of frequency bins per display by the number of range cells per display gives

$$\frac{\text{no. of frequency bins}}{\text{range cell}} = m.$$

Therefore, these two important parameters, number of range cells per display and the number of frequency bins per range cell, are very simply related to the sampling of the spectrum analyzer and can be easily changed. A special case is when the spectrum analyzer takes all of its samples on

one sweep. For our spectrum analyzer, this means $N = 1500$, $N/p = 500$, and $m = 1$. So there are 500 range cells and only one frequency bin per range cell; this is the range-only processing case. The other extreme of one range cell with 500 frequency bins is obtained by taking three samples per sweep and coherently processing over 500 sweeps. All values between these two extremes can be easily obtained.

The maximum unambiguous velocity is now easy to find since it is the displacement from a zero velocity point by an amount equal to half the number of frequency bins per range cell. The velocity of a target is $\lambda f_d/2$ where f_d is the Doppler frequency equal to the number of bins displacement from the zero velocity point times frequency per bin. The maximum unambiguous displacement is $m/2$, so that the maximum unambiguous velocity v_m is

$$v_m = \frac{\lambda}{2} \frac{m}{2} \delta .$$

This can be shown equal to $\lambda/4T$ as it must be.

The velocity resolution of the system can now be found by dividing the maximum unambiguous velocity by the number of velocity cells. This shows that the velocity resolution is $\delta\lambda/2$ m/s or equivalently, the Doppler frequency resolution is δ Hz.

V. CONCLUSIONS

FM-CW Doppler processing has two main advantages, simplicity and flexibility. The processing technique can be considered a special case of parallel correlators with frequency offset references. The requirement of linear FM modulation on the transmitted signal simplifies the parallel correlators to a single mixer and a single spectrum analyzer. The maximum range and range resolution are determined by the frequency sweep which is easily changed by a low level control voltage. The number of range cells, number of frequency bins per range cell, and the maximum unambiguous velocity is controlled by the sampling of the spectrum analyzer which is also easy to change.

VI. REFERENCES

- Barrick, D. E., FM-CW Radar Signals and Digital Processing, NOAA Technical Report ERL 283-WPL26, July 1973.
- Strauch, R. G., W. C. Campbell, R. B. Chadwick, and K. P. Moran, Microwave FM-CW Doppler Radar for Boundary Layer Probing, Geophysical Research Letters, Vol. 3, no. 3, p 193-196, March 1976.
- Chadwick, R. B., K. P. Moran, R. G. Strauch, G. E. Morrison, and W. C. Campbell, A New Radar for Measuring Winds, Bulletin of the American Meteorological Society, Vol. 57, no. 9, p 1120-1125, Sept. 1976.
- Cooper, G. R. and C. D. McGillem, Random Signal Radar, Technical Report EE67-11, Purdue University, Lafayette, Indiana, June 1967.
- Cooper, G. R., C. D. McGillem and W. B. Waltman, Use of Wideband Stochastic Signals for Measuring Range and Velocity, EASCON '69 Record, p 305-311, 1969.
- Chadwick, R. B. and G. R. Cooper, Measurement of Distributed Targets with the Random Signal Radar, IEEE Trans. on Aerospace and Electronic Systems, Vol. AES-8, no. 6, p 743-750, Nov. 1972.
- Strauch, R. G. and R. B. Chadwick, Measurement Capabilities of FM-CW Doppler Radars, 17th Conference on Radar Meteorology, American Meteorological Society, Oct. 1976.
- Strauch, R. G., Theory and Application of the FM-CW Doppler Radar, Ph.D. Thesis, University of Colo., 1976.

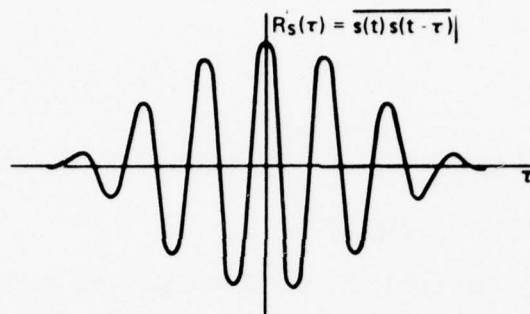


Figure 1. Autocorrelation function of transmitted signal.

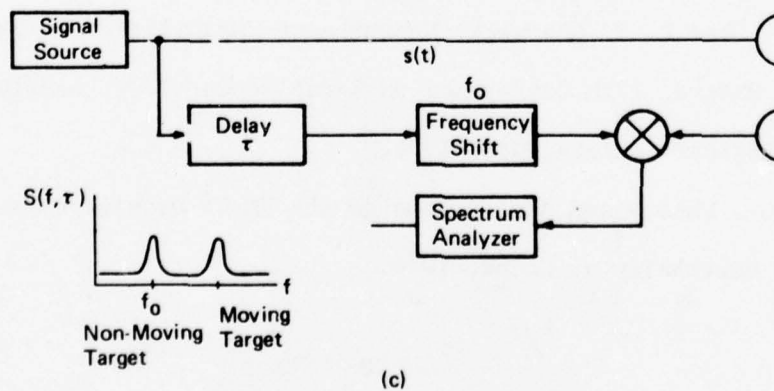
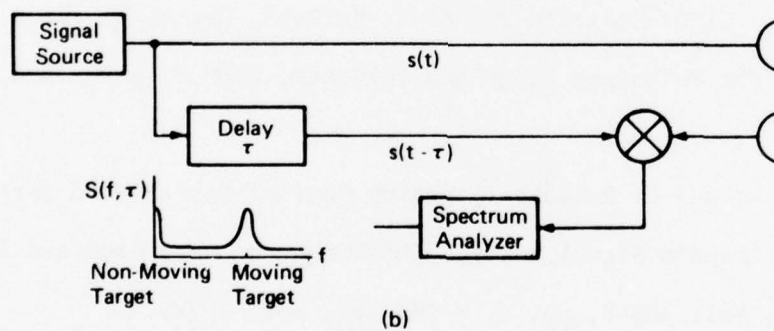
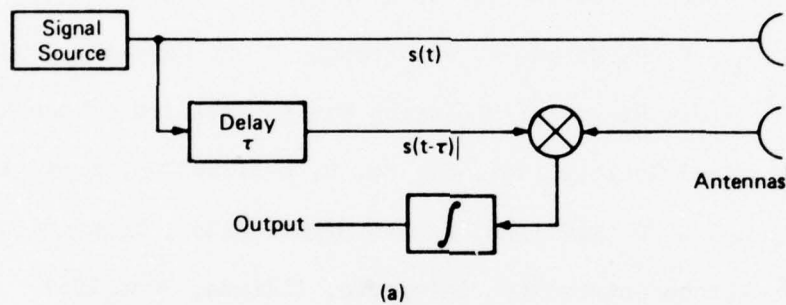


Figure 2(a). Conventional correlator. (b) Bandpass correlator.
(c). Bandpass correlator with frequency offset reference.

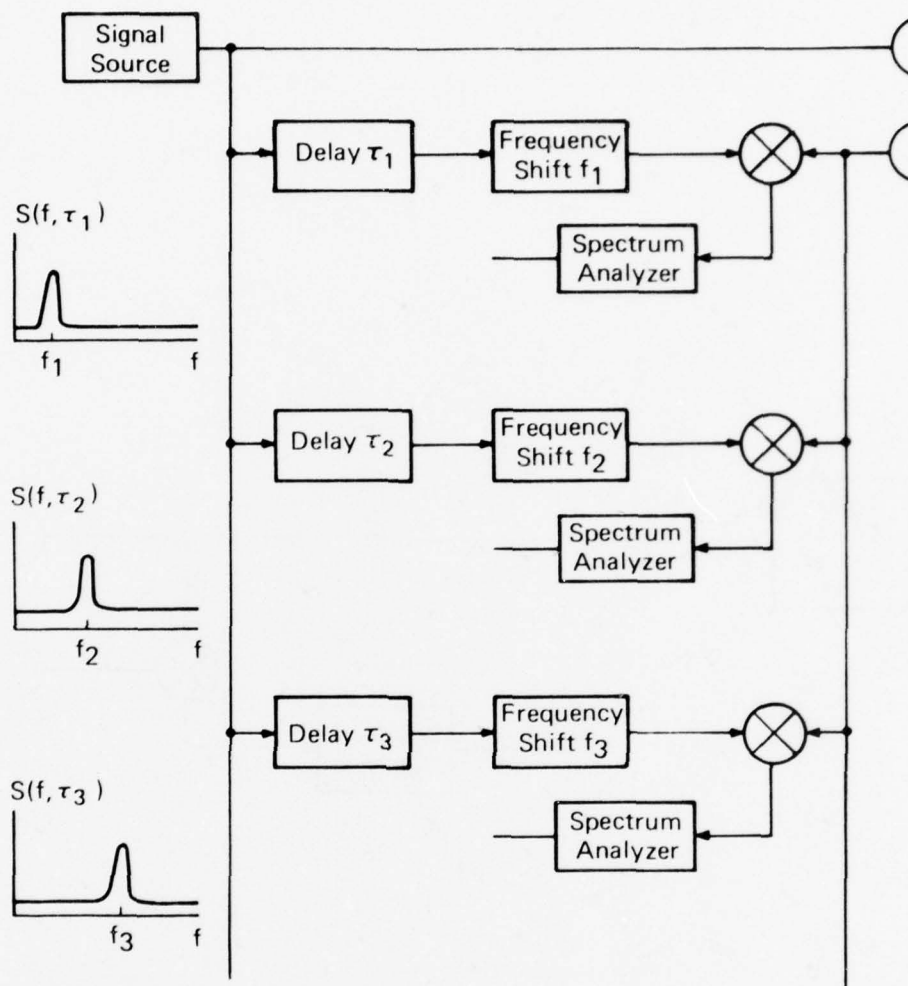


Figure 3. Parallel correlator receiver with non-moving target in each range cell.

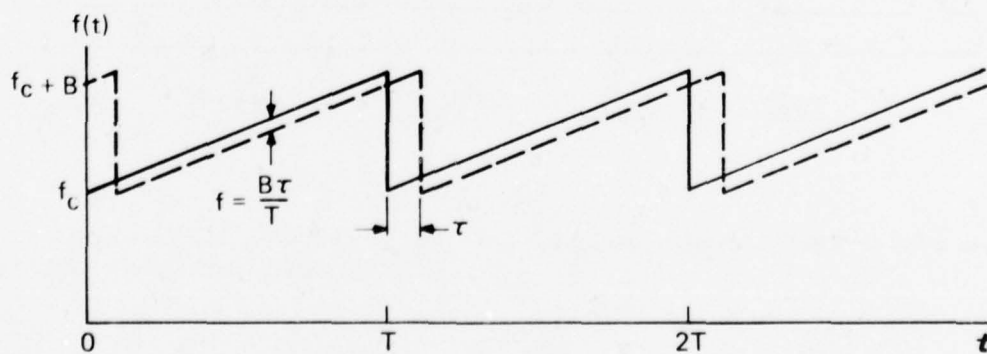
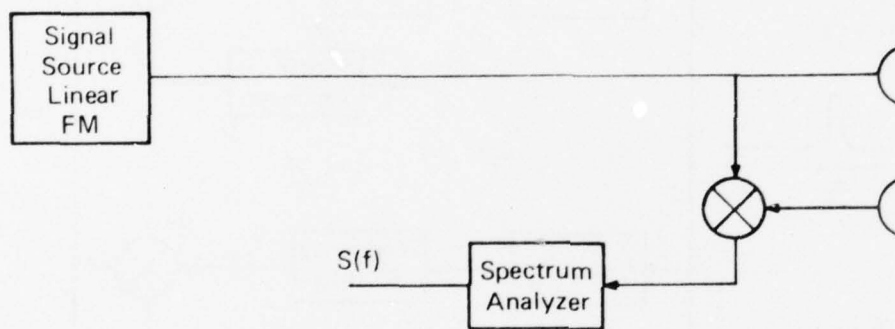
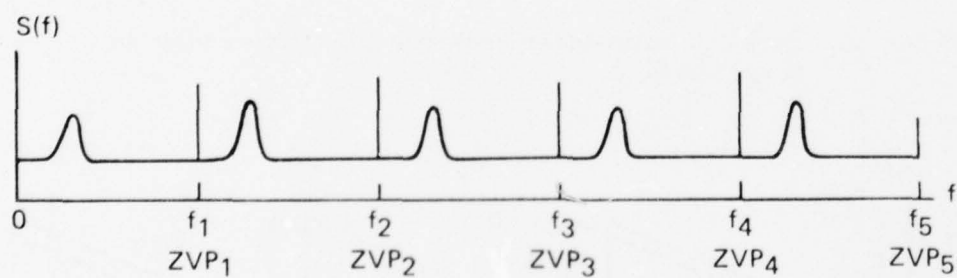


Figure 4. Frequency sweep for FM-CW radar.



(a)



(b)

Figure 5(a). FM-CW Doppler radar. (b) Radar output for five range cells with a moving target in each cell.

APPENDIX B. Required Frequency Stability to Suppress Ground Clutter

In Appendix A, it was pointed out that the FM-CW radar had no requirement on the phase of the transmitted signal, but there was a requirement on the starting frequency of the FM sweep. In this section, that requirement is quantified, and this allows us to determine maximum clutter suppression as function of range and instability.

A simplified block diagram of the FM-CW radar is shown in Fig. B-1. In this analysis, the amplitudes of the transmitted and received signal are not important and will be taken as unity. The transmitted signal for one sweep of length T is

$$s(t) = \sin 2\pi\phi_T(t) \quad 0 \leq t \leq T$$

$$\phi_T(t) = \frac{1}{2} \frac{B}{T} t^2 + f_o t$$

where the bandwidth is B Hz and the starting frequency is f_o Hz. Assume the return signal is from a point ground clutter target and has been delayed by τ so that

$$s(t-\tau) = \sin 2\pi\phi_T(t-\tau)$$

and the signal out of the mixer is then

$$r(t) = \cos 2\pi \phi_r(t)$$

$$\phi_r(t) = \phi_T(t) - \phi_T(t-\tau).$$

The phase term at the output of the mixer is then shown to be

$$\phi_r(t) = \frac{B}{T} t\tau - \frac{1}{2} \frac{B}{T} \tau^2 + f_o \tau.$$

So, during a sweep, $r(t)$ is a sinusoid with frequency proportional to the delay of the return signal, and with a phase equal to delay times RF sweep starting frequency. It is clear that any instability or jitter in this starting frequency will cause $r(t)$ to change from one sweep to the next, limiting the effectiveness of any device designed to cancel ground clutter.

To determine how much this frequency jitter will limit the maximum clutter suppression, we must find the spectrum of $r(t)$. For a single point clutter target at a certain range, $r(t)$ will be a sinusoid and if f_o has some jitter, this sinusoid will change phase randomly at time $T, 2T, \dots$. This is very much like the signal for a phase shift keyed (PSK) digital communication system. Lundquist (1969) has derived a very general expression for the power spectrum of a PSK signal $x(t)$ where

$$x(t) = V_c \cos(\omega_c t + \phi(t))$$

$$\phi(t) = \sum_{n=-\infty}^{\infty} a_n g(t-nT) .$$

Here, we are interested in the special case where $g(t) = 1$ for $0 \leq t \leq T$ and is zero elsewhere. Also we desire r phase levels, equidistant and equiprobable, i.e.,

$$a^{(k)} = \alpha_0 + \frac{k-1}{r} \alpha$$

$$\text{Prob}[a^{(k)}] = \frac{1}{r} .$$

It will be necessary to let r become infinite for this model to approximate our situation. The parameter α will then be the radian phase jitter in $r(t)$ due to the frequency jitter in f_0 .

The power spectrum of this PSK signal is

$$S(\omega_c + \omega) = \frac{V_c^2}{2} \left(\frac{T}{2\pi} \left[\frac{\sin(\frac{\omega T}{2})}{(\frac{\omega T}{2})} \right]^2 \left\{ 1 - \frac{F^2}{r^2} \right\} + \frac{F^2}{r^2} \delta(\omega) \right)$$

where
$$F \triangleq \frac{\sin(\frac{\alpha}{2})}{\sin(\frac{\alpha}{2r})} .$$

Note that there is a continuous part and a discrete part of this spectrum. The continuous part is due to the changes in phase of $r(t)$, which are caused by the jitter in sweep starting frequency, f_0 . So, the power in the

continuous spectrum can be called the jitter power, J, and the power in the discrete spectrum can be called the signal power, S. The signal power to jitter power ratio is then

$$\frac{S}{J} = \lim_{r \rightarrow \infty} \frac{F^2}{r^2 + F^2} .$$

To evaluate this limit, note that as r becomes large, the sine term in the denominator of F can be replaced by its argument. Then the r^2 terms in S/J will cancel leaving

$$\frac{S}{J} = \frac{A}{1-A} \quad \text{where} \quad A = \frac{\sin \alpha/2}{\alpha/2} .$$

The range of phase change of $r(t)$ is then proportional to the range of starting frequencies or the frequency jitter

$$\Delta\phi_r = 2\pi\tau\Delta f_o = \alpha .$$

The signal-to-jitter ratio can now be plotted as a function of the frequency jitter with delay as a parameter. This plot is Fig. B-2.

The main use of Fig. B-2 is to determine the maximum achievable clutter suppression. Since a clutter suppressor can only suppress signals with a discrete spectrum the signal-to-jitter ratio is the maximum clutter suppression that is achievable for that particular τ and Δf_o . For

example, if it is necessary to suppress ground clutter from 450 m range by 30 dB, the frequency jitter must be less than 8 kHz. The ground clutter suppressor that is presently under construction has a suppression potential of 48 dB. To achieve this for ranges of 450 m or less, a frequency stability of about 1 kHz is needed.

Reference

Lundquist, L. (1969), Digital PM Spectra by Transform Techniques, BSTJ, vol. 48. no. 2, p. 397-411.

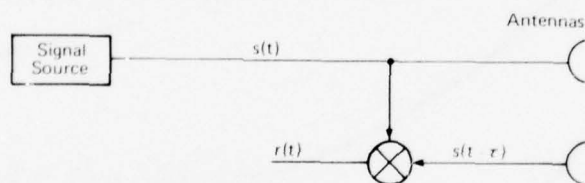


Figure B-1. Simple block diagram of FM-CW radar.

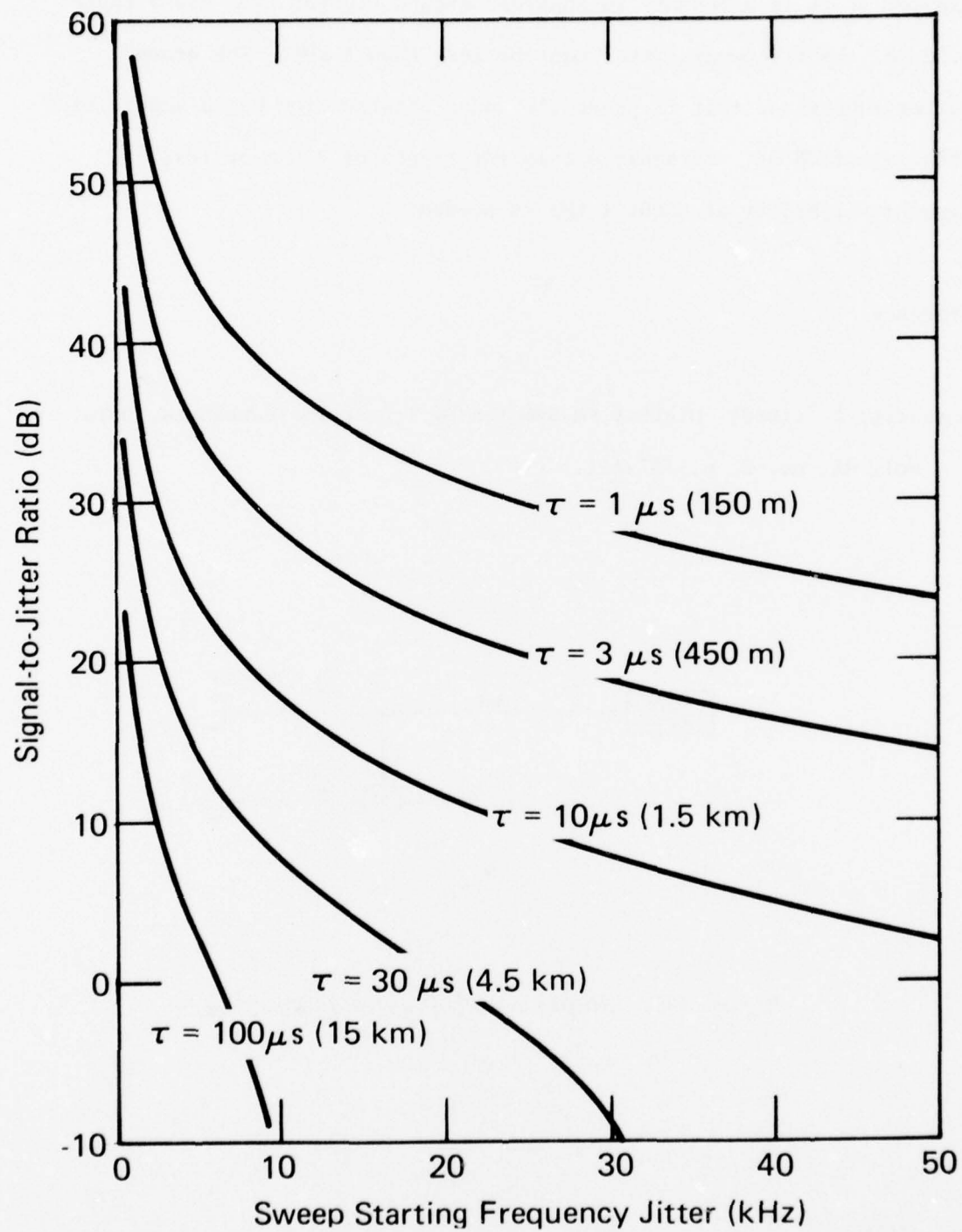


Figure B-2. Frequency stability required for a given signal-to-jitter ratio.

APPENDIX C. Comparison of Clutter Power for a Pulse Radar and a CW Radar

The wind shear problem requires operation at low elevation angles and short ranges. This appendix compares how easily two different radars can operate at low angles and short ranges by finding the ratio of return clutter powers. The critical aspect of operation at low elevation angles and short ranges is whether or not the receiver saturates. During the time the receiver is saturated by ground clutter, wind measurements are not possible. If the radars have similar first stages in the receivers, the results here tell which is the most susceptible to saturation.

Assume the geometry shown in Fig. C-1 where the antenna is h meters above the ground and looking at an elevation angle e . Let ϕ be the angle from antenna boresite and assume the antenna beam is

$$\begin{aligned} G(\phi) &= G_1 & |\phi| < e \\ &= G_1/\phi^{3/2} & |\phi| \geq e. \end{aligned}$$

The shape of the beam for angles less than the elevation angle is not important because this portion of the beam does not see the ground.

Assume that the ground has radar cross section per unit area of σ^0 . The incremental power returned from a incremental range element, dR at range R , in a plan view sector θ radians wide is

$$dP_c = \frac{P_T G^2(\phi) \sigma}{(4\pi)^3 R^4} \theta R dR$$

where P_T is the transmitted peak power. Since this is a comparison where a ratio of powers is formed, the common terms will cancel out. So rather than carry them along, we will drop them when they become multiplicative factors. The total clutter power can then be found by integrating over the illuminated range interval.

$$P_c = P_T \int_{R_1}^{R_2} \frac{G^2(\phi)}{R^3} dR$$

where terms that will eventually cancel have been dropped.

Because of the low elevation angle,

$$\phi \approx \frac{eR+h}{R}$$

and the clutter power expression becomes

$$P_c = P_T \int_{R_1}^{R_2} \frac{dR}{(eR+h)^3}$$

This integral evaluates to

$$P_c = \frac{P_T}{(eR_1+h)^2} - \frac{P_T}{(eR_2+h)^2}$$

For a CW radar the maximum illuminated range is infinite so the second term goes to zero. The minimum illuminated range can be taken as the smaller of the far-field boundary and the point at which the antenna beams intersect. Here the far-field boundary will be used. So the minimum illuminated range for the CW radar will be taken as

$$R_1' = D^2/\lambda .$$

Then, the ratio of clutter power for a pulse radar to that for a CW radar is given by,

$$\frac{P_c}{P_c'} = \frac{P_T}{P_T'} \left[\left(\frac{eR_1' + h}{eR_1' + h} \right)^2 - \left(\frac{eR_1' + h}{eR_2' + h} \right)^2 \right]$$

where primed terms are for the CW radar.

This ratio does not change greatly when e and h are changed over reasonable ranges (but, of course, the characteristics of a single specific radar do change as e and h are changed). The clutter power of a CW radar is independent of range cell while for a pulse radar the clutter power is approximately proportional to the range cell size. So this ratio varies with the range cell size. A plot of pulse clutter power over CW clutter power is shown in Fig. C-2 for some reasonable parameters. Whenever this ratio is positive in dB, the pulse clutter problem is more severe than the CW clutter problem.

This analysis is simplified because of the assumption of uniform reflectivity of the ground. Terrain with man-made objects is difficult to model and usually experimental techniques must be used. However, a conclusion of this appendix is that if the ground close to the radar is relatively smooth and free of man-made objects, an FM-CW radar will be easier to operate at short ranges and low elevation angles.

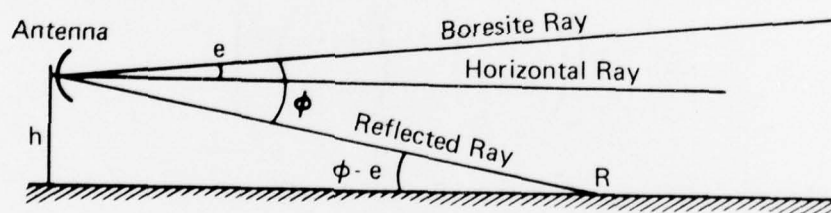


Figure C-1. Geometry for ground clutter comparison.

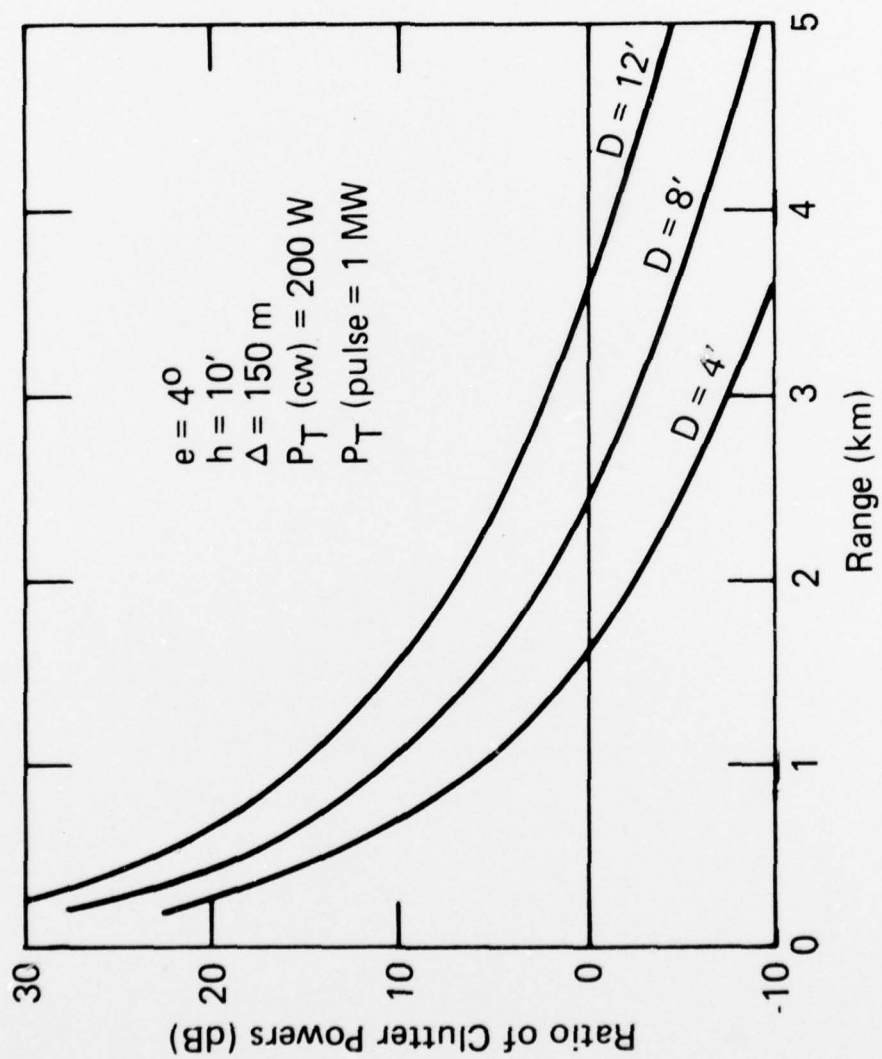


Figure C-2. Ratio of clutter power (pulse/CW) for various antenna diameters.

APPENDIX D. Histograms of C_n^2

This appendix gives probability histograms of the measured C_n^2 values for each of the nine height bins. The histograms are presented two different ways; first on a monthly basis and then on an hour of day basis. The numbers represent the percentage of time the measured C_n^2 was within that bin. A number of .000 indicates the percentage of time was less than .0005, but greater than zero. A blank indicates that the percentage of time was zero.

For the last four months of the experiment, the radar was located in an urban area where the ground clutter was large. So, the lower two height intervals could not be used.

The hour-of-day (MST) histograms are presented in a similar format, except only one height bin, 805 m, is included. The data obtained in the last four months of the experiment were not used for the hour-of-day histograms.

A more convenient way of looking at this data is used in Section 3.

2. n

	10^{-12}	10^{-13}	10^{-14}	10^{-15}	10^{-16}	10^{-17}	10^{-18}									
Mar	.053	.003	.001	.000	.001	.117	.334	.286	.131	.056	.019	.003	.001	.000	.000	.000
Apr			.001	.002	.016	.070	.155	.253	.268	.149	.074	.011	.002	.001	.000	.000
May			.000	.024	.143	.310	.288	.151	.041	.020	.015	.007	.000	.001	.000	.000
June	.000	.000	.001	.002	.014	.042	.131	.307	.242	.098	.077	.057	.015	.003	.001	.000
July		.000	.002	.006	.009	.017	.067	.239	.405	.209	.040	.003	.001	.001	.001	.000
Aug		.000	.001	.004	.010	.035	.147	.234	.280	.235	.040	.006	.002	.001	.000	.000
Sept		.000	.000	.002	.024	.143	.465	.297	.042	.008	.007	.002	.002	.005	.001	.000
Oct			.001	.002	.065	.351	.397	.137	.042	.003	.001	.001	.001	.001	.001	.000

TABLE D.2 Monthly probability C_n^2 histograms at height 322 m

	10^{-12}	10^{-13}	10^{-14}	10^{-15}	10^{-16}	10^{-17}	10^{-18}
Mar		.050 .005 .002 .001 .001 .000 .003 .090 .186 .220 .180 .143 .083 .024 .007 .002 .001 .001					
Apr			.002 .000 .011 .057 .114 .198 .203 .209 .148 .048 .011 .001 .001 .001 .001 .001 .001 .000				
May			.002 .047 .123 .233 .237 .174 .106 .045 .019 .008 .003 .001 .000 .000 .000 .000 .000 .000				
June	.000 .000 .000 .001 .005 .027 .057 .154 .249 .200 .133 .074 .065 .017 .006 .005 .001 .000 .000						
July		.000 .001 .003 .004 .006 .018 .033 .061 .171 .271 .275 .117 .029 .006 .002 .000 .000 .000					
Aug		.000 .002 .005 .009 .010 .024 .039 .149 .271 .284 .148 .045 .006 .002 .001 .000 .000 .000					
Sept			.000 .001 .008 .047 .129 .354 .315 .114 .017 .002 .001 .000 .000 .000 .000 .000 .000 .000				
Oct				.001 .003 .043 .146 .313 .349 .098 .032 .012			

TABLE D.3 Monthly probability C_n^2 histograms at height 483 m

10^{-12}	10^{-13}	10^{-14}	10^{-15}	10^{-16}	10^{-17}	10^{-18}
Mar	.049 .006 .001 .001 .000 .000 .028 .111 .195 .209 .146 .161 .064 .015 .005 .002 .001 .000					
Apr	.000 .002 .002 .002 .046 .083 .129 .189 .197 .192 .103 .041 .011 .003 .001 .001 .001 .000					
May	.000 .000 .021 .076 .155 .247 .185 .150 .098 .047 .013 .003 .002 .000 .000 .000 .000 .000					
June	.000 .000 .002 .004 .011 .037 .085 .202 .219 .182 .110 .074 .038 .011 .009 .002 .000 .000					
July	.000 .000 .003 .006 .007 .011 .028 .046 .113 .208 .246 .235 .083 .011 .002 .001 .000 .000					
Aug	.000 .000 .002 .004 .007 .010 .017 .026 .068 .221 .274 .181 .135 .041 .005 .002 .000 .000					
Sept	.000 .000 .005 .021 .090 .192 .339 .248 .071 .015 .004 .001 .001 .000 .000 .000 .000 .000					
Oct	.001 .001 .001 .012 .082 .206 .417 .205 .054 .017 .002					
Nov	.024 .019 .100 .172 .363 .194 .075 .027 .011 .005 .004 .001					
Dec	.006 .029 .056 .088 .161 .302 .298 .038 .011 .003 .002					
Jan	.068 .147 .199 .290 .197 .076 .011 .004 .003 .001					
Feb	.004 .062 .174 .383 .278 .090 .007 .001 .001 .000					

TABLE D.4 Monthly probability C_n^2 histograms at height 644 m

	10^{-12}	10^{-13}	10^{-14}	10^{-15}	10^{-16}	10^{-17}	10^{-18}											
Mar	.046	.007	.003	.000	.000	.011	.044	.095	.194	.235	.167	.126	.061	.019	.006	.002	.001	.000
Apr		.000	.002	.001	.009	.064	.095	.131	.204	.206	.172	.075	.025	.009	.004	.003	.000	.000
May				.001	.024	.085	.174	.237	.180	.137	.097	.042	.011	.006	.002	.001	.000	
June	.000	.001	.002	.007	.022	.041	.091	.215	.210	.162	.104	.081	.034	.019	.007	.001	.000	.000
July	.000	.004	.006	.008	.013	.030	.055	.112	.205	.233	.216	.094	.020	.002	.000	.000		
Aug	.000	.002	.004	.008	.011	.020	.026	.061	.183	.283	.197	.126	.055	.014	.002	.001	.000	
Sept				.000	.001	.006	.032	.132	.253	.283	.203	.066	.021	.007	.008	.001	.000	.000
Oct					.001	.006	.014	.089	.161	.319	.257	.098	.037	.008	.005	.001	.000	
Nov						.000	.029	.021	.035	.166	.350	.237	.091	.030	.012	.007	.006	.002
Dec								.001	.019	.042	.083	.164	.198	.291	.150	.025	.010	.002
Jan									.006	.292	.065	.219	.207	.122	.052	.019	.007	.004
Feb									.001	.036	.127	.447	.296	.074	.016	.002	.001	.000

TABLE D.5 Monthly probability C_n^2 histograms at height 805 m

	10^{-12}	10^{-13}	10^{-14}	10^{-15}	10^{-16}	10^{-17}	10^{-18}										
Mar	.047	.007	.003	.000	.011	.045	.095	.174	.235	.167	.126	.061	.019	.006	.002	.001	.000
Apr		.001	.001	.002	.029	.073	.101	.136	.198	.144	.071	.026	.011	.007	.001	.000	.000
May			.000	.004	.040	.106	.208	.244	.170	.129	.065	.020	.010	.002	.001	.000	
June	.000	.003	.008	.022	.046	.130	.222	.205	.146	.097	.058	.032	.020	.005	.001	.000	.000
July		.001	.005	.007	.010	.019	.040	.062	.125	.236	.240	.167	.065	.017	.003	.002	.000
Aug	.000	.003	.005	.010	.012	.021	.034	.071	.197	.261	.191	.120	.048	.012	.005	.001	.000
Sept			.000	.002	.011	.065	.170	.234	.263	.154	.056	.017	.006	.004	.004	.000	
Oct				.005	.010	.034	.093	.197	.282	.161	.093	.062	.043	.011	.001		
Nov					.024	.016	.019	.076	.218	.265	.208	.098	.028	.012	.019	.002	
Dec							.000	.004	.035	.106	.161	.236	.248	.122	.041	.011	.001
Jan								.004	.220	.273	.227	.133	.082	.030	.012	.012	.000
Feb								.001	.036	.268	.506	.165	.021	.001	.001		

TABLE D.6 Monthly probability C_n^2 histograms at height 966 m

	10^{-12}	10^{-13}	10^{-14}	10^{-15}	10^{-16}	10^{-17}	10^{-18}										
Mar	.052	.004	.001	.000	.000	.021	.048	.115	.231	.227	.133	.103	.047	.012	.004	.000	.000
Apr			.001	.006	.031	.076	.104	.136	.180	.184	.140	.080	.029	.018	.008	.002	
May			.000	.008	.040	.091	.167	.230	.172	.117	.076	.043	.023	.010	.006	.002	.000
June	.000	.000	.002	.018	.047	.110	.216	.190	.151	.103	.081	.038	.022	.007	.002	.001	.000
July	.001	.005	.008	.011	.023	.041	.068	.112	.220	.226	.160	.084	.025	.008	.005	.001	.000
Aug	.000	.000	.003	.005	.010	.012	.020	.039	.076	.179	.243	.186	.123	.054	.020	.009	.004
Sept			.000	.003	.019	.072	.131	.226	.263	.155	.070	.027	.010	.005	.003	.000	
Oct				.000	.013	.010	.035	.086	.224	.195	.173	.111	.068	.036	.025	.004	
Nov					.029	.015	.035	.137	.195	.244	.178	.092	.032	.012	.014	.003	
Dec							.001	.008	.036	.133	.158	.258	.200	.104	.034	.011	.005
Jan							.000	.003	.250	.212	.239	.184	.068	.020	.008	.006	.001
Feb							.000	.005	.031	.236	.499	.174	.034	.013	.006	.001	.001

TABLE D.7 Monthly probability C_n^2 histograms at height 1127 m

	10^{-12}	10^{-13}	10^{-14}	10^{-15}	10^{-16}	10^{-17}	10^{-18}											
Mar	.053	.004	.001	.000	.009	.067	.109	.173	.187	.160	.120	.061	.028	.015	.004	.003	.001	.000
Apr			.002	.010	.046	.087	.115	.158	.208	.182	.106	.051	.016	.009	.003	.001		
May			.002	.013	.043	.093	.164	.199	.155	.114	.079	.047	.022	.017	.008	.005	.000	
June		.002	.007	.021	.050	.117	.193	.197	.149	.112	.080	.033	.021	.006	.002	.001	.000	
July	.002	.006	.009	.012	.029	.045	.073	.116	.204	.220	.145	.078	.033	.013	.005	.001	.000	
Aug	.000	.001	.004	.007	.010	.012	.022	.041	.088	.185	.220	.180	.106	.055	.018	.030	.001	
Sept		.001	.005	.026	.080	.139	.219	.227	.148	.073	.036	.011	.013	.002	.000			
Oct			.010	.010	.009	.037	.114	.225	.148	.121	.099	.036	.128	.004				
Nov				.001	.031	.019	.048	.151	.200	.270	.128	.049	.051	.034	.003			
Dec						.003	.009	.066	.131	.125	.163	.186	.132	.061	.031	.002		
Jan						.001	.002	.056	.260	.097	.232	.227	.077	.022	.008	.005		
Feb						.002	.012	.044	.227	.349	.198	.085	.028	.020	.008	.001		

TABLE D.8 Monthly probability C_n^2 histograms at height 1288 m

	10^{-12}	10^{-13}	10^{-14}	10^{-15}	10^{-16}	10^{-17}	10^{-18}										
Mar	.058	.000	.000	.000	.024	.053	.103	.180	.154	.167	.138	.060	.032	.017	.004	.002	.000
Apr		.000	.003	.010	.040	.084	.114	.143	.203	.190	.112	.046	.027	.010	.003	.001	.000
May		.000	.003	.012	.038	.082	.176	.207	.182	.136	.078	.038	.015	.009	.004		
June		.000	.001	.005	.017	.045	.111	.184	.217	.165	.118	.074	.035	.014	.008	.001	.000
July	.000	.002	.006	.009	.015	.029	.050	.072	.104	.176	.218	.153	.083	.038	.017	.007	.002
Aug	.000	.001	.004	.007	.011	.022	.043	.076	.173	.204	.183	.110	.057	.031	.028	.005	.000
Sept		.000	.001	.004	.026	.071	.129	.204	.220	.156	.083	.035	.021	.014	.002	.000	
Oct		.002	.013	.004	.004	.009	.034	.211	.165	.098	.107	.087	.059	.113	.017		
Nov				.001	.033	.022	.108	.091	.188	.266	.124	.047	.033	.035	.009		
Dec					.000	.001	.003	.010	.063	.139	.137	.224	.178	.107	.047	.025	.001
Jan						.002	.003	.006	.019	.269	.355	.216	.088	.019	.009	.005	
Feb						.003	.007	.027	.222	.344	.189	.096	.039	.031	.006	.004	

TABLE D.9 Monthly probability C_n^2 histograms at height 1449 m

	10^{-12}	10^{-13}	10^{-14}	10^{-15}	10^{-16}	10^{-17}	10^{-18}										
Mar	.057	.008	.000	.001	.035	.057	.134	.150	.155	.151	.127	.057	.025	.020	.005	.003	.001
Apr		.000	.006	.013	.038	.078	.107	.140	.204	.186	.113	.047	.029	.012	.006	.001	
May		.000	.007	.017	.035	.080	.156	.199	.183	.125	.080	.043	.026	.008	.002	.000	
June		.000	.001	.005	.017	.043	.104	.183	.221	.159	.108	.074	.045	.019	.006	.002	.000
July	.000	.003	.006	.011	.015	.034	.053	.069	.106	.164	.200	.157	.084	.041	.022	.004	.001
Aug	.000	.001	.004	.008	.011	.014	.025	.043	.077	.150	.201	.172	.112	.061	.046	.039	.001
Sept	.000	.000	.002	.006	.029	.068	.124	.189	.213	.155	.083	.038	.035	.025	.001		
Oct		.006	.010	.002	.010	.032	.240	.117	.099	.111	.075	.102	.131	.001			
Nov				.006	.031	.037	.124	.122	.284	.182	.092	.031	.029	.043	.001		
Dec					.000	.001	.005	.022	.091	.139	.138	.179	.143	.128	.043	.020	.004
Jan					.002	.005	.007	.305	.029	.146	.194	.170	.070	.016	.022	.002	
Feb							.002	.007	.024	.180	.391	.168	.068	.052	.017	.001	.001

TABLE D.10 Hour-of-day histograms for C_n^2 at height 805 m

	10^{-12}	10^{-13}	10^{-14}	10^{-15}	10^{-16}	10^{-17}	10^{-18}										
0	.010	.001	.004	.011	.057	.106	.180	.169	.195	.137	.072	.038	.017	.001	.001	.000	
1	.010	.002	.004	.011	.039	.118	.190	.185	.174	.138	.059	.039	.025	.003	.001	.000	
2	.010	.001	.007	.017	.025	.109	.175	.173	.164	.151	.082	.060	.014	.004	.004	.001	
3	.010	.006	.004	.010	.035	.095	.175	.160	.155	.138	.102	.077	.021	.005	.004	.001	
4	.002	.010	.002	.001	.003	.033	.088	.122	.169	.166	.175	.117	.078	.022	.008	.003	.001
5	.010	.000	.000	.004	.020	.043	.094	.166	.196	.173	.133	.102	.033	.014	.005	.001	
6	.010	.000		.006	.009	.036	.061	.134	.181	.220	.167	.085	.049	.019	.010	.000	.000
7	.010	.001	.003	.004	.009	.040	.048	.132	.188	.243	.135	.075	.058	.022	.017	.001	.000
8	.010	.000	.000	.004	.007	.030	.081	.120	.191	.251	.166	.069	.042	.016	.009	.001	
9	.011				.003	.037	.093	.114	.241	.229	.131	.075	.034	.014	.005	.001	
10	.012	.001		.001	.010	.048	.138	.170	.273	.167	.080	.048	.014	.012	.003	.000	
11	.012	.001	.000	.000	.007	.049	.127	.318	.239	.167	.089	.040	.024	.018	.004	.000	
12	.010	.002	.001	.003	.011	.055	.123	.242	.272	.145	.065	.045	.017	.004	.002	.001	.000
13			.001	.009	.019	.061	.141	.215	.281	.163	.076	.021	.006	.003	.001	.000	
14		.000	.002	.016	.064	.118	.224	.288	.149	.091	.024	.005	.003	.001			.000

TABLE D.10 Hour-of-day histograms for C_n^2 at height 805 m (continued)

10^{-12}	10^{-13}	10^{-14}	10^{-15}	10^{-16}	10^{-17}	10^{-18}												
15	.000	.002	.028	.044	.111	.165	.243	.263	.090	.022	.010	.007	.007	.000	.001			
16	.000	.004	.006	.003	.026	.046	.119	.154	.239	.222	.109	.040	.017	.009	.004	.001	.000	
17	.004	.001	.000	.006	.032	.063	.137	.139	.197	.199	.138	.051	.025	.012	.003	.001		
18	.004	.004	.001	.002	.015	.049	.128	.159	.189	.208	.140	.062	.032	.003	.002	.001		
19	.006	.002	.001	.005	.010	.028	.102	.193	.208	.219	.136	.063	.021	.005	.001	.000		
20				.004	.023	.065	.154	.025	.185	.186	.096	.055	.023	.003	.001	.000		
21	.008	.001	.002	.003	.027	.124	.178	.211	.179	.130	.068	.035	.024	.005	.001	.001	.000	.000
22	.000	.011	.003	.004	.008	.029	.120	.189	.197	.164	.134	.078	.043	.016	.002	.001	.001	
23		.010	.003	.004	.010	.046	.124	.202	.182	.168	.131	.068	.036	.010	.003	.001		